Contents lists available at ScienceDirect

Materials Today Bio

journal homepage: www.journals.elsevier.com/materials-today-bio

Photothermal-enhanced silver nanocluster bioactive glass hydrogels for synergistic antimicrobial and promote wound healing

Fuqiang Song [a,c,d], Anqi Ye [a,c], Linyuan Jiang [a,c], Yang Lu [c], Yanzhen Feng [c], Rong Huang [a,c], Siting Du [c], Xiaoyu Dong [c], Ting Huang [c], Ping Li [c], Liangliang Yang [a,d], Jinjing Zhang [a,**], Mengjia Xu [b,***], Li Cheng [a,****], Jian Xiao [c,d,*]

[a] Affiliated Cixi Hospital, Cixi Biomedical Research Institute, Wenzhou Medical University, Ningbo, 315300, China
[b] Ningbo Key Laboratory of Biomedical Imaging Probe Materials and Technology, Zhejiang International Cooperation Base of Biomedical Materials Technology and Application, Ningbo Cixi Institute of Biomedical Engineering, Laboratory of Advanced Theranostic Materials and Technology, Ningbo Institute of Materials Technology and Engineering, Chinese Academy of Sciences, Ningbo 315201, China
[c] Department of Wound Healing, The First Affiliated Hospital of Wenzhou Medical University, Wenzhou, Zhejiang, 325035, China
[d] Oujiang Laboratory (Zhejiang Lab for Regenerative Medicine, Vision and Brain Health), School of Pharmaceutical Sciences, Wenzhou Medical University, Wenzhou, Zhejiang, 325035, China

ARTICLE INFO

ABSTRACT

Antibacterial hydrogels are promising for combating infections and promoting wound healing. Nevertheless, excessive antibiotics induce resistance, and high metal ion levels cause cytotoxicity, complicating healing. Here, we introduce a hydrogel incorporating polydopamine-coated bioactive glass (BGs@PDA) on reduced graphene oxide (rGO) with photothermal therapy (PTT) and silver nanoclusters (AgNCs) for synergistic antibacterial treatment. This design enables rapid bacterial eradication and controlled release. Near-infrared-assisted heating provides noninvasive, targeted hyperthermia, killing bacteria quickly. Post-PTT addition of low-dose AgNCs reduces toxicity while enhancing antimicrobial efficacy and biocompatibility. BGs@PDA-loaded rGO prevents sedimentation, improves photothermal conversion and conductivity, and stabilizes the hydrogel structure. Constructed from chitosan and hydroxyethyl cellulose, the hydrogel is cross-linked by PDA and rGO, enhancing mechanical strength, adhesion, self-healing, free radical scavenging, and continuous wound exudate absorption. PDA encapsulation facilitates BGs degradation, improving the wound microenvironment. In vivo studies confirm accelerated healing and potent synergistic antibacterial effects, indicating its potential as a low-dose, antibiotic-free alternative for clinical wound infection management.

1. Introduction

As the body's main protective barrier, the skin is continually exposed to external conditions, rendering it highly vulnerable to both physical and chemical harm [1,2]. The process of wound healing generally involves four interrelated stages: hemostasis, inflammation, proliferation, and tissue remodeling. These phases collaborate to reestablish the protective barrier [3,4]. When a large wound is untreated or exposed to air for an extended period, the moist micro-environment at the wound site inevitably leads to bacterial infection [5,6]. Various wound dressings, including foams [7], nanofibers [8,9], sponges [10,11], and hydrogels [12] have been developed to address this problem. Among these, hydrogels are particularly promising due to their three-dimensional network structure that mimics the extracellular matrix, high absorptivity for wound exudates, significant moisture retention, oxygen permeability, and flexible shape adaptability for drug delivery [3,4,13,
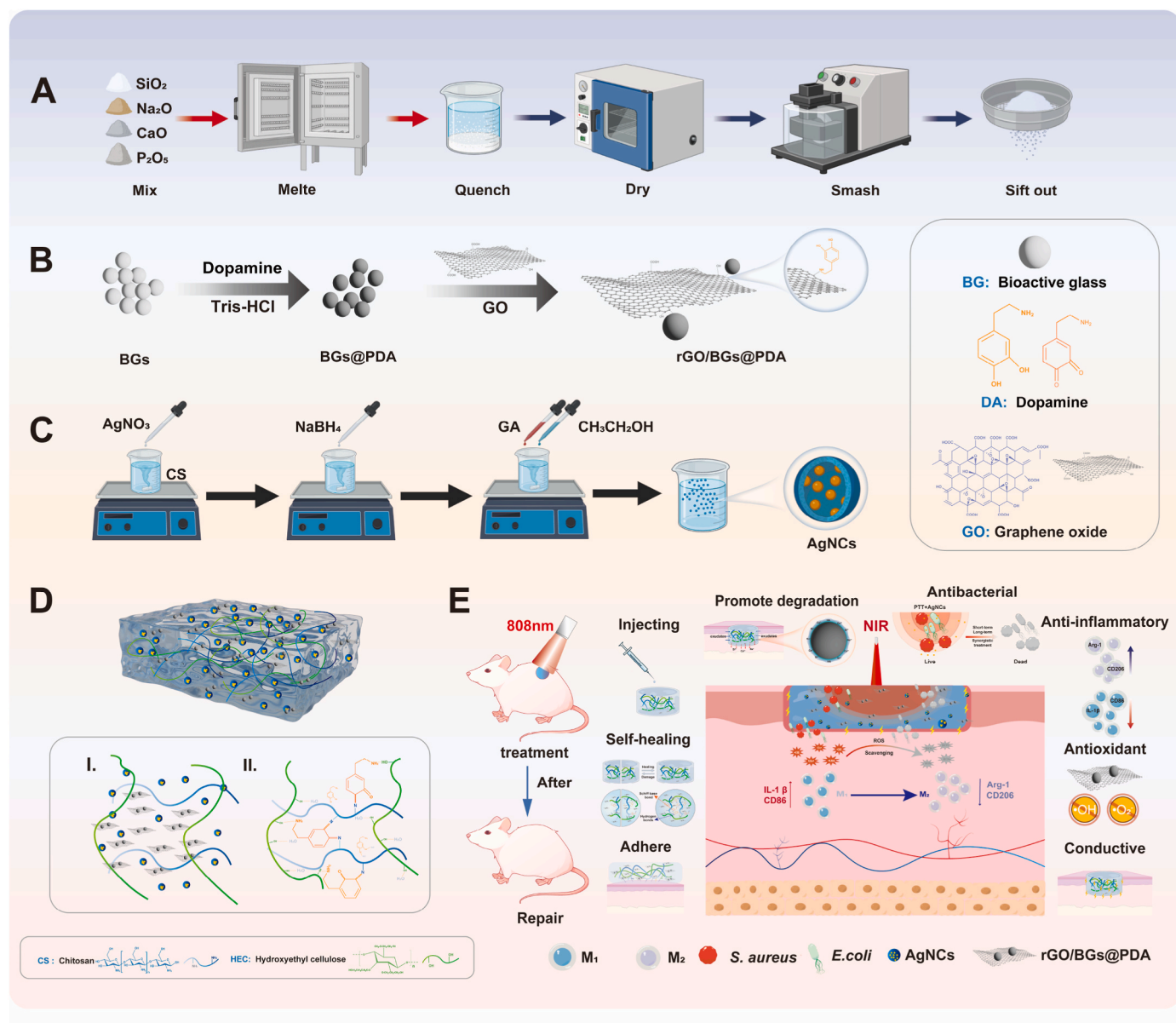
Scheme 1. Schematic illustration of formation and application of rGO/BGs@PDA loaded CS-HEC/AgNCs hydrogel for wound healing. **(A)** Synthesis of BGs. **(B)** Synthesis illustration of BGs@PDA and loaded on GO (rGO/BGs@PDA). **(C)** Synthesis of chitosan stabilized AgNCs. **(D)** Characteristics of hydrogels as well as local enlargements of composition (I) and the detailed crosslinking between the individual components (II). **(E)** Diagram of the mechanism of the hydrogel in wound healing.

14]. Antibiotics-free antimicrobial functionalized hydrogels have garnered significant interest because the common clinical use of antibiotics often results in drug resistance [15,16]. Therefore, developing innovative therapeutic technologies to combat bacterial infections and enhance the wound healing process is of paramount importance.

Compared to traditional antimicrobial therapies, photothermal therapy (PTT) mediated hydrogels reduce antibiotic overuse by converting light energy into heat via photothermal agents that effectively kill bacteria [17–19]. In addition, PTT has several advantages in wound repair, including the absence of spatial limitations, high tissue penetration, and non-invasive application [20–22]. While PTT effectively eliminates most bacteria through temperature-responsive properties, it does not provide long-term, slow-release sterilization during wound healing [23,24]. Ag nanomaterials possess potent antibacterial properties by releasing Ag ions and generating reactive oxygen species. Silver nanoclusters (AgNCs) are smaller and safer than traditional silver nanoparticles, offering significant antimicrobial effects and unique

fluorescence imaging capabilities for non-invasive, real-time wound healing monitoring [25,26]. However, AgNCs tend to agglomerate during synthesis and require stabilizers for dispersion. While proteins and peptides are common stabilizers, they can result in larger particle sizes [26,27]. On the contrary, as a natural polysaccharide chitosan (CS) with excellent biosafety and degradability, it can be used as an ideal stabilizer to produce AgNCs with controllable particle size, enabling the development of novel core-shell hybrid materials [27,28].

Bioactive glass (BGs), a widely adopted biomaterial in tissue repair, has shown significant potential in promoting wound healing [29,30]. BGs are usually in contact with body fluids for degradation, and hydrogels can continuously absorb wound exudate, making them ideal carriers for BGs and providing a better environment for their degradation. However, their degradation is still slow, which can lead to prolonged contact with skin tissue and trigger an inflammatory response. Polydopamine (PDA), a photothermal agent in PTT, is synthesized through the oxidative self-polymerization of dopamine. Its abundant

catechol structure enhances hydrogel adhesion by forming hydrogen bonds with water molecules [31]. Due to its inherent excellent biocompatibility, antioxidant and antimicrobial properties, coupled with its unique catechol structure, PDA can be used not only as a photothermal agent in PTT, but also extensively in biomaterials as a bio-coating that can be used with negligible cytotoxicity. In addition, encapsulation of BGs with PDA can effectively regulate the degradation rate of BGs, reduce the accumulation of residual materials, and improve the cellular interface, thus minimizing cytotoxicity [32–34]. Previous studies have indicated that the multiple physiological functions of BGs are closely related to their conversion into hydroxyapatite-like structures, a process significantly facilitated by PDA coating [6]. However, our preliminary results revealed that PDA-coated BGs (BGs@PDA) tended to deposit before gelling, leading to inhomogeneous gelation due to their larger particle size. Introducing graphene oxide (GO) provides a promising solution. GO, rich in oxygen-containing functional groups such as epoxides and carboxyl groups, can engage in redox reactions with PDA. This interaction facilitates the loading of BGs@PDA onto GO, resulting in rGO/BGs@PDA during oxidation [35,36]. This GO integrated strategy offers a novel method for delivering large sedimentable bioactive materials with higher homogeneity and a superior photothermal conversion capability compared to PDA. As a natural polysaccharide, chitosan not only serves as a stabilizer for reducing AgNCs but also, due to its amino and hydroxyl functional groups, can form physical or chemical bonds with PDA, GO, and H_2O. This makes it widely used in hydrogel drug delivery systems [37–39]. However, the use of single-component chitosan hydrogels is limited in promoting skin wound healing due to their inherently low mechanical strength [39,40]. In contrast, as a non-ionic water-soluble polymer, hydroxyethyl cellulose (HEC) can significantly enhance the mechanical strength and toughness of hydrogels [41]. HEC also enhances interactions between polymer chains, which remain stable at elevated temperatures, thus boosting the thermal stability crucial for photothermal hydrogels [42,43]. As shown in Scheme 1, during hydrogel formation, PDA can form Schiff base bonds with CS. The abundant hydroxyl groups in both PDA and HEC facilitate hydrogen bonding, enhancing the mechanical strength and adhesion properties of the hydrogels [42,44]. The quinone groups in PDA can interact through redox reactions with the epoxy and hydroxyl groups on GO's surface, resulting in a more stable structure. Additionally, hydrogen bonds can also form between the hydroxyl and amine groups in PDA and the hydroxyl and carboxyl groups on reduced-rGO [45]. The aromatic groups in PDA can stack with the aromatic carbon ring of rGO through π–π interactions [36,46]. The interactions between these components are responsible for the improvement and maintenance of the mechanical strength and stability of the hydrogel.

In summary, this study designed multifunctional BGs-loaded photohydrothermal hydrogels with enhanced antibacterial efficiency for wound healing applications. The combined effect of PTT and AgNCs successfully prevents bacterial growth and treats wound infections. Leveraging the redox properties of PDA and GO, BGs@PDA were uniformly loaded onto rGO via chemical bonds, ensuring homogeneous dispersion and enhancing GO's conductivity. The introduction of rGO significantly improved the photothermal conversion efficiency of the hydrogel, enabling rapid temperature response under light exposure and enhancing its antibacterial effect. BGs@PDA not only offered essential structural support but also enhanced cell proliferation and tissue regeneration at the wound site, thereby accelerating the healing process. Overall, this composite hydrogel combines the advantages of various functional materials, demonstrating excellent mechanical properties, thermal stability, biocompatibility, and antibacterial activity, and holds great potential for clinical wound care applications.

2. Materials and methods

2.1. Materials

Silicon dioxide (SiO_2), calcium oxide (CaO), sodium oxide (Na_2O), phosphorus pentoxide (P_2O_5), graphene oxide (GO), dopamine hydrochloride (DA), chitosan (MW: 800–1000), chitosan (deacetylated 95 %), hydroxyethylcellulose (low viscosity), sodium β-glycerophosphate, 2,2-Biphenyl-1-picrylhydrazyl (DPPH) were purchased from Maclean's (Shanghai, China). Sodium borohydride ($NaBH_4$), Silver nitrate ($AgNO_3$), ethylenediaminetetraacetic acid (EDTA), anhydrous ethanol, glutaraldehyde (GA), acetic acid (CH_3COOH) were purchased from Sinopharm (Shanghai, China).

2.2. Synthesis of bioactive glasses

The material applied in this study was melt-derived BioGlass® 45S5 with the following composition (wt%): 45 % SiO_2, 24.5 % Na_2O, 24.5 % CaO and 6 % P_2O_5. The production of 45S5 BGs was carried out by a melting process [47]. Specifically, the precursor raw materials were homogeneously mixed and then melted at high temperatures (>1200 °C) and quenched to form an amorphous glass. The desired bioactive glass was synthesized by drying, pulverizing, and sieving after cooling to room temperature.

2.3. Synthesis of silver nanoclusters

Based on previous work, silver nanoclusters were synthesized using CS as a stabilizer with slight modifications [27]. Briefly, 100 mg of CS (MW: 800–1000) and EDTA were added to 5 mL of $AgNO_3$ (0.5 mM) solution and stirred until the solution was completely dissolved. $NaBH_4$ (1.0 mM) solution was then added to the solution and stirred adequately, then ethanol was added until the solution changed from clear to cloudy. Glutaraldehyde (25 %) was added to the solution, centrifuged after stirring and lyophilized.

2.4. Preparation of BGs@PDA and rGO/BGs@PDA

DA (1 g) was added to 100 mL of Tris-HCl solution and stirred at room temperature until the color of the solution changed from clear to dark brown, then BGs were added and stirred overnight to prepare BGs@PDA. The BGs@PDA were purified by centrifugation until the supernatant became clear and dried at 65 °C for 24h.

An aqueous solution of GO was added and dispersed by ultrasound to the above BGs@PDA. The IR spectra of GO and rGO/BGs@PDA were compared to verify whether BGs@PDA were loaded onto GO through redox reactions.

2.5. Synthesis of composite hydrogels

1.5 % chitosan and 0.15 % hydroxyethyl cellulose were dissolved in a solution containing 0.1 M acetic acid and stirred overnight. 4 mg of AgNCs and rGO/BGs@PDA were added to the solution and mixed well. Then 200 mg of sodium β-glycerophosphate was added under an ice bath and refrigerated.

The Fourier transform infrared spectrometer (FTIR, Thermo Fisher, IS 50, USA) characterized the hydrogels. The morphology of the hydrogels was observed using SEM (FEI, QUANTA250, USA) and Micro CT (Skyscan1276, BRUKER, USA). For details of the procedure, see SI (Supplementary Information).

2.6. Injectability and gelation time

Injectability was investigated first by macroscopic observation by inhaling the hydrogel into a syringe and observing whether the hydrogel could be punched through the syringe and filled into different shapes. To
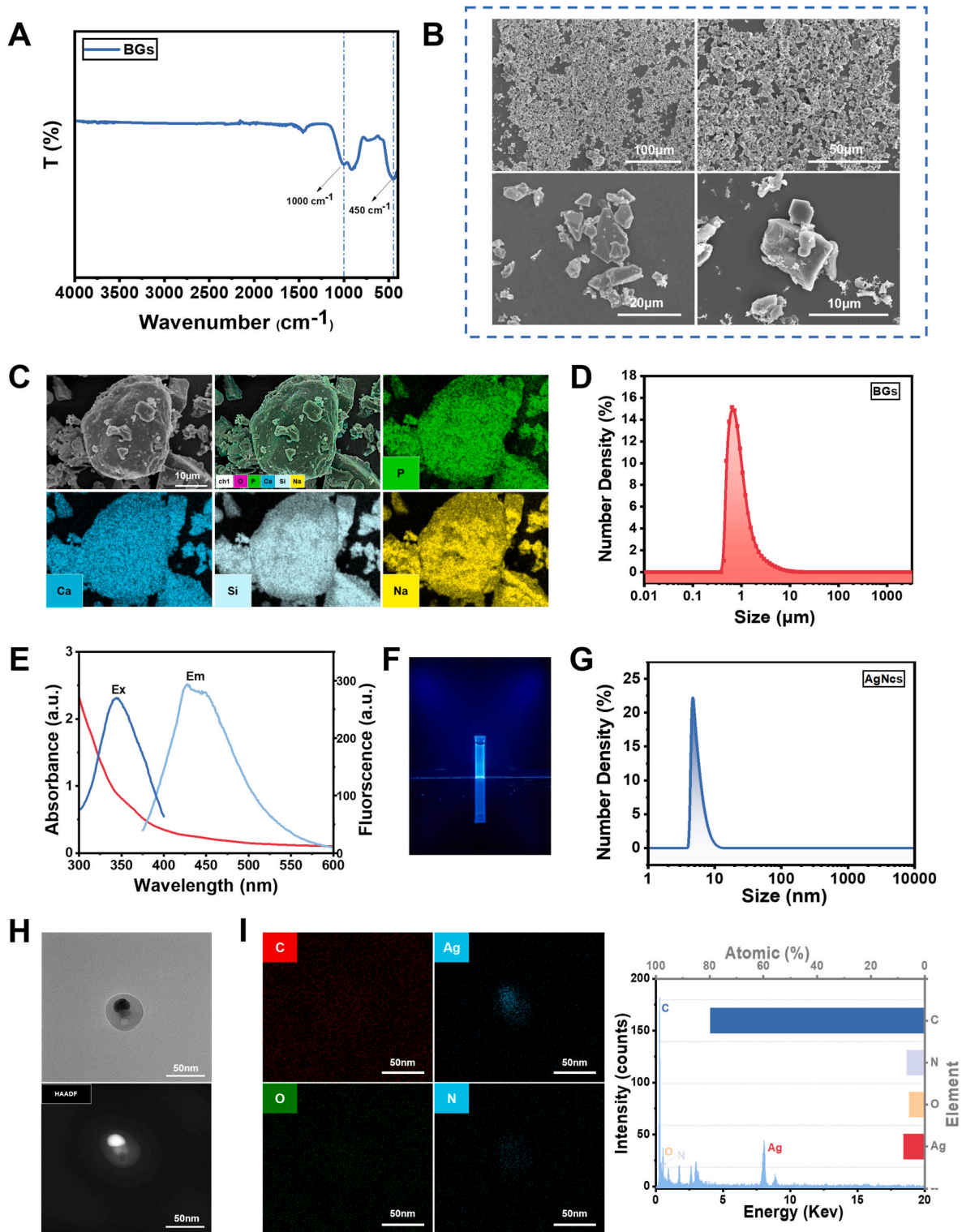
Fig. 1. Characterization of BGs and AgNCs. **(A)** Infrared spectra of BGs. **(B)** SEM micrographs of bioactive glass at 500x, 1000x, 2000x, and 5000× magnifications, with scales of 100 μm, 50 μm, 20 μm, and 10 μm, respectively. **(C)** Elemental mapping analysis of BGs (P in green; Ca in cyan; Si in gray; Na in yellow). **(D)** Particle size distribution of bioactive glass measured by laser diffraction. **(E)** UV and fluorescence spectra of AgNCs. **(F)** Fluorescence effect diagram of AgNCs emitted under 300 W UV irradiation (305 nm). **(G)** Particle size analysis diagram of AgNCs. **(H)** Chitosan-coated AgNCs nano microspheres in bright field and dark field state with a scale bar of 50 nm. **(I)** The elemental mapping analysis of AgNCs reveals the distribution of C (red), Ag (blue), O (green), and N (cyan), the scale bar is 50 nm. Additionally, the EDX spectrum for figure H is provided.

verify whether the hydrogel exhibits shear thinning properties, we can utilize a rheometer (Waters, HR-2, USA) to experiment by observing the changes in its viscosity as the shear rate varies from 0.01 s^{-1}–1000 s^{-1}.

The test tube inversion method was used to evaluate the gel formation experiments. Specifically, the hydrogel was bottled and placed in a

37 °C constant temperature incubator and recorded by tilting it at a certain angle every 15 s for observation. The gelation process was considered complete when the gel solution no longer flowed within 30 s of turning.
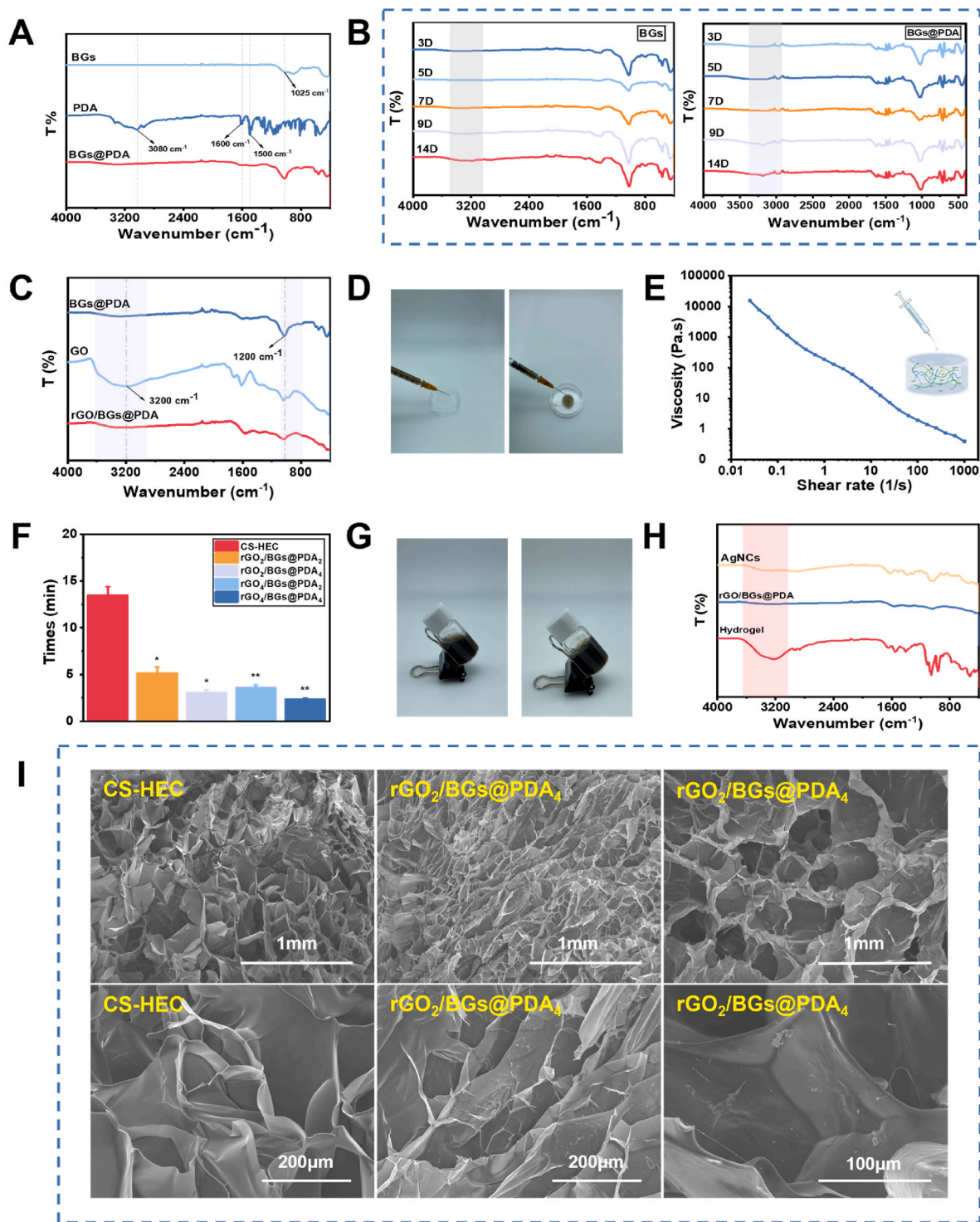

Fig. 2. Characterization of BGs, BGs@PDA, rGO/BGs@PDA and hydrogels. **(A)** Comparison of infrared spectra of BGs, PDAs, and BGs@PDA. **(B)** Infrared spectra of BGs and BGs@PDA immersed in SBF-simulated body fluids for 3, 5, 7, 9, and 14 days. **(C)** Infrared spectra of GOs and BGs@PDA loaded rGO. **(D)** Hydrogel injectability analysis through a syringe. **(E)** Hydrogel shear-thinning rheology experiments. **(F)** Hydrogel formation time of different compositions. **(G)** Hydrogel inversion experiment. **(H)** Infrared spectra of composite hydrogel. **(I)** The morphological characteristics of the CS-HEC hydrogel were depicted under 50x and 200× magnifications, with scale bars of 1 mm and 200 μm, respectively. Meanwhile, the SEM images of the rGO$_2$/BGs@PDA$_4$ hydrogel were presented at 50x (showing different regions), 200x, and 500× magnifications, with scale bars of 1 mm, 1 mm, 200 μm, and 100 μm, respectively. *P < 0.05, **P < 0.01, ***P < 0.001.

2.7. Adhesion, stretch, self-healing properties, and mechanical strength

The adhesion, stretch, self-healing properties and mechanical strength of the hydrogel can be found in the SI.

2.8. Water content, swelling ratio, stability, and degradability

Detailed experimental procedures for water content, swelling ratio, stability, and degradability of the hydrogel are given in the SI.

2.9. DPPH radical scavenging assay and measuring electrical conductivity

Hydrogel free radical scavenging was evaluated using 2,2-biphenyl-1-picrylhydrazyl (DPPH) [12]. The exact procedure is described in SI.

To evaluate the conductivity of different hydrogels, their resistivity R was measured separately using a resistivity tester (Suzhou Jingge, ST2242, China).

Resistance to conductivity formula: G = 1/R

2.10. Hydrogel photothermal experiments

The detailed procedures for the photothermal experiments of the hydrogel can be found in the SI.

2.11. Cytocompatibility and blood compatibility of hydrogel

To assess the cytocompatibility and hemocompatibility of the hydrogels, extracts were prepared by incubating 200 μL of hydrogels in DMEM medium and sterile PBS at 37 °C for 24 h.

Cell experiments were conducted using NIH 3T3 cells, obtained from the Cell Resource Center, Shanghai Institutes for Life Sciences, Chinese Academy of Sciences. The experiments included a cytotoxicity assay using CCK-8, a cell scratch assay, and a cell live/dead staining assay. Detailed procedures were available in the SI.

Blood compatibility experiments were then performed with the hydrogel extract in PBS. The exact procedure is described in SI.

2.12. In vitro antimicrobial test

The detailed procedure was provided in the SI.

2.13. In vivo wound healing assessment

It was decided to use hydrogels containing $GO_2/BGs@PDA_4$ for the subsequent animal experiments. The detailed procedure is described in SI.

H&E staining and Masson staining were employed to evaluate healing effects. For detailed procedures, refer to the SI.

2.14. Immunofluorescence at wound site

The evaluation of inflammation at the wound location throughout different stages of healing was conducted. *In vivo*, immunofluorescence analysis was carried out using IL-1, CD86, Arg-1, and CD206 markers. The exact procedure is described in SI.

2.15. Statistical analysis

All experiments were carried out across a minimum of three separate trials. The data are shown as the mean $\pm$ standard deviation. To evaluate statistical significance, one-way ANOVA was employed, with P values represented as follows: * <0.05, ** <0.01, *** <0.001, **** <0.0001; "ns" indicates no significant differences.

3. Results and discussion

3.1. Characterization of BGs and silver nanoclusters

After the synthesis of 45S5 BGs, the average weight percent of oxides was analyzed by XRF, with results presented in Table S1. The results indicated that the average chemical composition of each sample was consistent with the known composition of 45S5 within the preparation tolerances [48]. The IR spectrogram of BGs was shown in Fig. 1A, in which the characteristic absorption peaks of phosphate and Si-O-Si asymmetric stretching vibration were located at 450 cm^{-1} and 1000 cm^{-1}, respectively. The Si-O bond formed the basis of the 45S5 silicate network framework, and its appearance served as a key indicator for the successful synthesis of BGs [49]. The morphology of BG particles was analyzed using scanning electron microscopy (SEM) at various magnifications. As shown in Fig. 1B, the particles exhibit an overall irregular shape and a relatively uniform particle size. The results of the EDS analysis were shown in Fig. 1C, which indicated that the four elements of Si, Na, Ca, and P were uniformly distributed in the BGs particles. All these results confirmed the successful synthesis of BGs and indicated their homogeneity and consistency. The detailed analysis of the particle size was conducted using a laser particle size analyzer to determine the number distribution and volume density. The analysis revealed that the number density of BGs was primarily concentrated within the range of 2–10 μm, with a D50 value of 0.81 μm (Fig. 1D). The volume density, on the other hand, was distributed between 0.4 μm and 110 μm, with a D50 value of 10.7 μm (Fig. S1).

The UV absorption and fluorescence spectra of AgNCs were shown in Fig. 1E. The AgNCs exhibited a strong absorption peak at 350 nm in the UV absorption spectrum. This phenomenon could be attributed to the discrete energy level structure due to their ultrafine size [28,50]. The fluorescence spectroscopy analysis showed that AgNCs exhibited fluorescence peaks at an excitation wavelength (E_x) of 350 nm and an emission wavelength (E_m) of 450 nm. As shown in Fig. 1F, the AgNCs were able to emit blue fluorescence when irradiated with a 300 W UV light (305 nm). This phenomenon confirmed the optical activity of AgNCs and further supported their potential application as fluorescent probes in monitoring the wound healing process [51]. As shown in Fig. 1G, the particle size of AgNCs nano microspheres synthesized using chitosan as a stabilizer was mainly concentrated in the range of 20–45 nm by DLS analysis. The sample's morphology was examined using Talos TEM, revealing that AgNCs were consistently enclosed within chitosan microspheres, as observed in both light and dark fields (Fig. 1H and Fig. S2). Furthermore, EDS analysis revealed that elemental Ag was surrounded by elemental nitrogen (N) in chitosan, which confirms the effective encapsulation and stabilization role of chitosan in the synthesis of AgNCs (Fig. 1H and I). These results demonstrated the successful synthesis of AgNCs using chitosan as a stabilizing agent.

3.2. Characterization of BGs@PDA and rGO/BGs@PDA

In this study, the strategy of coating the surface of BG with a layer of PDA was adopted to enhance the bioactivity of the BGs within the hydrogel and promote cell attachment [6]. The IR spectrums of BGs and BGs@PDA in Fig. 2A showed that the Si-O-Si telescopic vibrational peaks were both observed around 1025 cm^{-1}, which was a typical characteristic peak of silicate-based BGs. Notably, BGs@PDA also exhibited the characteristic absorption peaks of PDA at 1500 cm^{-1} and 1600 cm^{-1}, corresponding to the backbone vibration of the benzene ring and the stretching vibration of the carbonyl group (C=O), respectively. In addition, BGs@PDA exhibited a stronger hydroxyl (O-H) stretching vibration peak at 3400 cm^{-1}, further confirming the successful introduction of the PDA coating and the consequent significant effect on the chemical bond between BGs and PDA.

It has been demonstrated that BGs can enhance the release of several cytokines from cells, such as basic fibroblast growth factor (bFGF) and
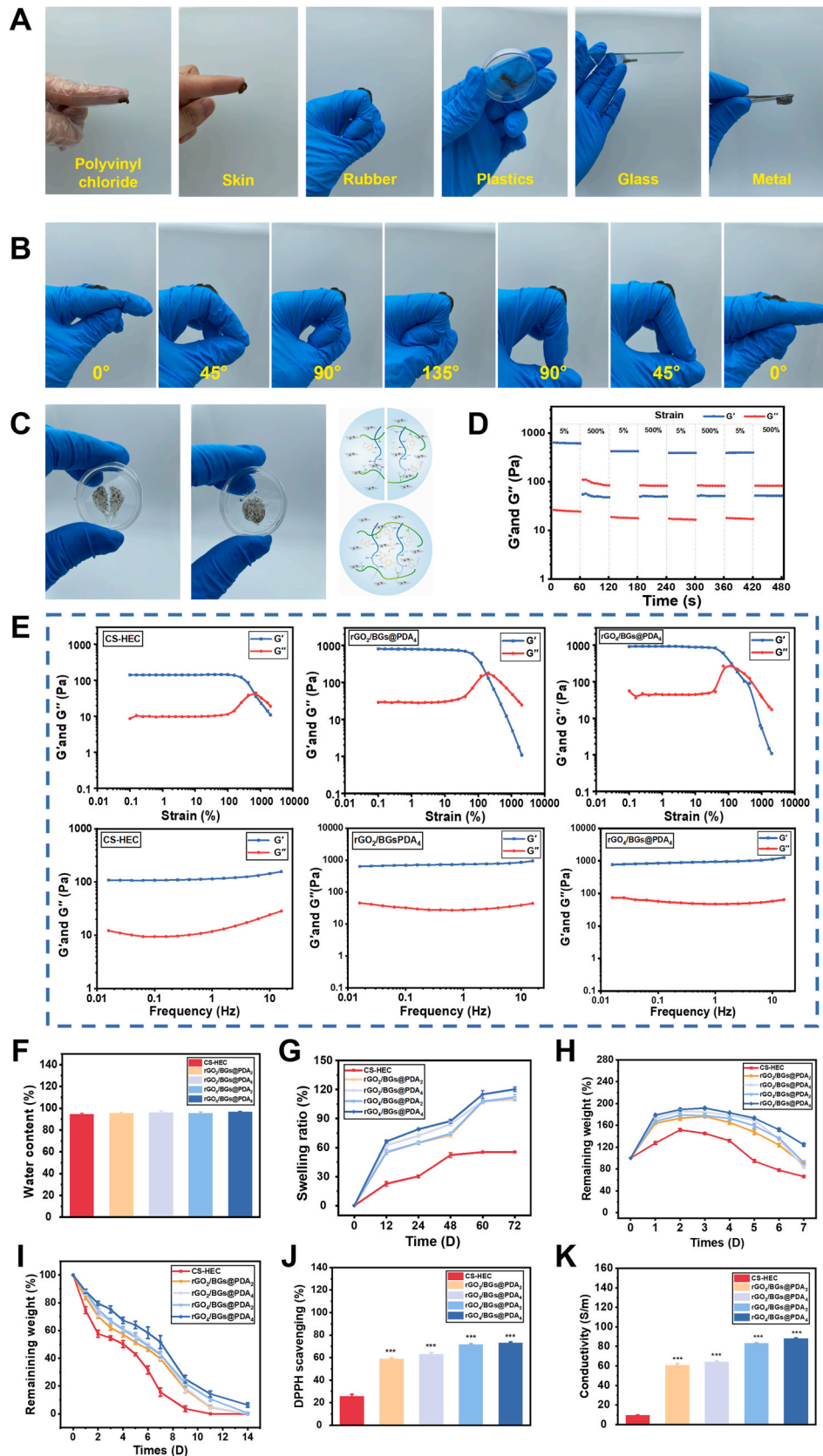
Fig. 3. Characterization of hydrogel. **(A)** Photographs of hydrogels adhering to different matrix materials. **(B)** The softness of rGO/BGs@PDA hydrogels. **(C)** Schematic representation of the macroscopic self-healing property of the hydrogel. **(D)** Hydrogel cyclic strain experiments. **(E)** CS-HEC, rGO$_2$/BGs@PDA$_4$, rGO$_4$/BGs@PDA$_4$ hydrogels fixed at a frequency of 1 HZ for stress scanning and fixed at a stress of 5 % for frequency scan. **(F)** Water content analysis of the hydrogel. **(G)** Swelling rate of the hydrogel. **(H)** Stability of the hydrogel. **(I)** Degradation rate of the hydrogel. **(J)** DPPH scavenging rate of the hydrogel. **(K)** Electrical conductivity of the hydrogel. *P < 0.05, **P < 0.01, ***P < 0.001.

vascular endothelial growth factor (VEGF), which in turn facilitates the process of wound healing. This stimulatory effect is closely associated with converting BGs to hydroxyapatite (HA) [34,45]. As a biomaterial coating, PDA exhibits excellent low cytotoxicity. When applied to BGs, PDA effectively accelerates the degradation of BGs, which in turn promotes the conversion of BGs to hydroxyapatite (HA), thereby optimizing the biocompatibility and bioactivity of the biomaterial. To further verify the promotive effect of PDA on the conversion of BGs to HA, an investigation was conducted by immersing the samples in simulated body fluid and comparing the appearance time points of the O-H stretching vibration peaks in IR spectra which illustrated the conversion of HA. In Fig. 2B, the PDA-coated BGs showed the O-H stretching vibration peak appeared two days earlier than that of BGs without PDA wrapping. Nevertheless, in Fig. S3, it was observed in the preliminary experiments that BGs@PDA was susceptible to sedimentation behavior during the gel formation process. To enable BGs@PDA to be uniformly dispersed in solution before gelation, graphene oxide (GO) was introduced into the system and improved the dispersibility significantly. Taking advantage of the fact that GO was reductive after polymerization, it was possible to load BGs@PDA on it after reduction [52,53]. By comparing the IR spectra of BGs@PDA and rGO/BGs@PDA (Fig. 2C), the results revealed that the vibrational peaks of the hydroxyl group of GO, which appear very broad at 3200 cm^{-1}, are attenuated after reaction with PDA to form a bond. The stretching vibration peaks of the epoxy bonds corresponding to GO in the range of 1220-1050 cm^{-1} disappeared after the ring-opening reaction with the amino group on PDA to form covalent bonds. The vibrational peak of the Si-O bond at 1020 cm^{-1} representing the BGs did not change. Thus, BGs@PDA was loaded on GO by redox reaction successfully. This platform also provided a feasible idea for hydrogel delivery of large-particle, easy-to-precipitate drugs through wrapping with reductive coatings followed by chemical reactions assisted loading to nanomaterials that can improve dispersity.

3.3. Characterization of rGO/BGs@PDA loaded CS-HEC/AgNCs hydrogel

It is important that the dressing fits and completely covers irregularly shaped wounds. Hydrogels with injectable properties can be a good solution to this problem [54]. The hydrogel could be injected through a syringe in Fig. 2D. Rheological experiments on the rGO$_2$/BGs@PDA$_4$ hydrogel also verified the relationship between the viscosity and the shear rate of the hydrogels. Fig. 2E illustrates that as the shear rate increased from 0.1 S^{-1}–1000 S^{-1}, the viscosity of the hydrogel decreased, demonstrating its excellent shear-thinning behavior and feasible injectability.

The inversion method using test tubes was utilized to determine the gelation duration of the hydrogel. The formation times for various hydrogels were as follows: CS-HEC at 13.5 $\pm$ 0.92 min, rGO$_2$/BGs@PDA$_2$ at 5.16 $\pm$ 0.63 min, rGO$_2$/BGs@PDA$_4$ at 3.08 $\pm$ 0.29 min, rGO$_4$/BGs@PDA$_2$ at 3.58 $\pm$ 0.29 min, and rGO$_4$/BGs@PDA$_4$ at 2.33 $\pm$ 0.14 min (Fig. 2F and G). As the content of BGs@PDA and rGO in the hydrogel system increased, there was a significant reduction in cross-linking time. In particular, the elevated rGO content enhances the density of cross-links, which also contributes to a shorter crosslinking duration. The IR spectra of the hydrogel exhibited the formation of very broad O-H peaks at 3000 cm^{-1} -3500 cm^{-1} in Fig. 2H, indicating the presence of numerous hydrogen bonds within the system.

The morphology of the CS-HEC/AgNCs hydrogel and rGO/BGs@PDA hydrogel were analyzed by SEM. As shown in Fig. 2I, both CS-HEC and rGO/BGs@PDA hydrogels exhibited rich and uniformly distributed porous structures. This porous and homogeneous architecture provides an ideal microenvironment for drug delivery and cell adhesion while maintaining excellent breathability, which is crucial for oxygen supply and the removal of metabolic waste during the wound healing process. In contrast, the unloaded CS-HEC hydrogel presented a smoother surface, whereas the rGO/BGs@PDA-modified hydrogel displayed a

rougher texture and revealed the network structure formed by rGO. Subsequently, Micro-CT was employed to separately analyze the structure of the rGO/BGs@PDA hydrogel, and the results showed that its cross-section remained porous (Fig. S34). Additionally, due to the different compositions of the hydrogels, varying levels of contrast were observed under X-ray irradiation, clearly displaying the distribution of BGs within the hydrogel. These structural characteristics suggest that rGO/BGs@PDA hydrogels possess potential advantages in biomedical applications, particularly in promoting wound healing.

Hydrogel with adhesive properties can protect the wound during the healing process, isolating it from external contact while promoting tight binding of the drug to the wound, thereby stimulating cells to produce a variety of factors to accelerate healing [55]. The synthesized hydrogels were able to achieve effective adhesion to a wide range of different surface materials including skin in Fig. 3A, proving the versatility of hydrogel in the multipurpose application. Particularly noteworthy was that the hydrogel adhered to the skin surface and was difficult to dislodge even after light shaking. The superior adhesive properties of the hydrogel may be related to the presence of PDA. PDA contains a high number of reducible functional groups, such as catechol and amino groups, which enable PDA to form various physical and chemical interactions with the skin, including π-π stacking and hydrogen bonding. These interactions enhance the adhesive performance of the hydrogel. Given the flexibility and stretchability of healthy skin, hydrogel dressings must have adequate stretch properties [56]. For this purpose, we simulated the range of motion of the finger joints from 0° flexion to 135° for testing. As illustrated in Fig. 3B, the hydrogel successfully returned to its initial size and form after being flexed from 0° to 135° and then returning to 0°, which demonstrates the hydrogel's excellent elongation and fatigue resistance characteristics.

In practical applications, hydrogels may deform or fracture during extrusion, increasing the risk of wound infection when used as dressings without self-healing properties [57]. To assess the hydrogel's capacity for self-healing, macroscopic self-healing experiments were conducted. Results indicated that the cut hydrogel quickly adhered upon contact. Cyclic stress tests using a rheometer demonstrated that the hydrogel could recover to its original elastic modulus (G′) and loss modulus (G″) after four cycles of 5 % and 500 % stress (Fig. 3C and D). The superior self-healing property of rGO/BGs@PDA contained hydrogel may stem from the catechol groups on the PDA which promote the rapid formation of hydrogen bonds with water molecules upon maturation [58,59].

The mechanical properties of CS-HEC, rGO$_2$/BGs@PDA$_4$, and rGO$_4$/BGs@PDA$_4$ hydrogels were also characterized. As shown in Fig. 3E, both rGO$_2$/BGs@PDA$_4$ and rGO$_4$/BGs@PDA$_4$ hydrogels exhibit a significant increase in G′ and G″ compared to CS-HEC hydrogel and the differences between rGO$_2$/BGs@PDA$_4$ and rGO$_4$/BGs@PDA$_4$ hydrogels were not significant. This phenomenon may be attributed to the introduction of GO into the hydrogel, which formed a rich cross-linking network, resulting in a significant increase in G′ and G″, while the rGO$_2$/BGs@PDA$_4$ hydrogel had reached a saturated state within its cross-linking network. In this case, even a further increase in the content of GO could not significantly affect the mechanical properties of the hydrogel [60–62].

As shown in Fig. 3F, the hydrogels water contented of CS-HEC, rGO$_2$/BGs@PDA$_2$, rGO$_2$/BGs@PDA$_4$, rGO$_4$/BGs@PDA$_2$, and rGO$_4$/BGs@PDA$_4$ were 94.53 $\pm$ 0.89 %, 95.45 $\pm$ 0.77 %, 95.93 $\pm$ 1.54 %, 95.42 $\pm$ 1.34 %, 96.56 $\pm$ 0.69 %, respectively. These results showed that the synthesized hydrogels all possess water content comparable to that of the extracellular matrix and all exceeding 90 %, which was important for simulating the extracellular matrix microenvironment to promote cell attachment and growth [63]. Furthermore, the hydrogels' swelling properties facilitate the absorption of wound exudate, maintaining a moist environment at the wound site and creating optimal conditions for healing. Additionally, the high-water content of the hydrogel provides a favorable environment for BGs, thereby accelerating the degradation rate of BGs. As shown in Fig. 3G, the swelling property of CS-HEC
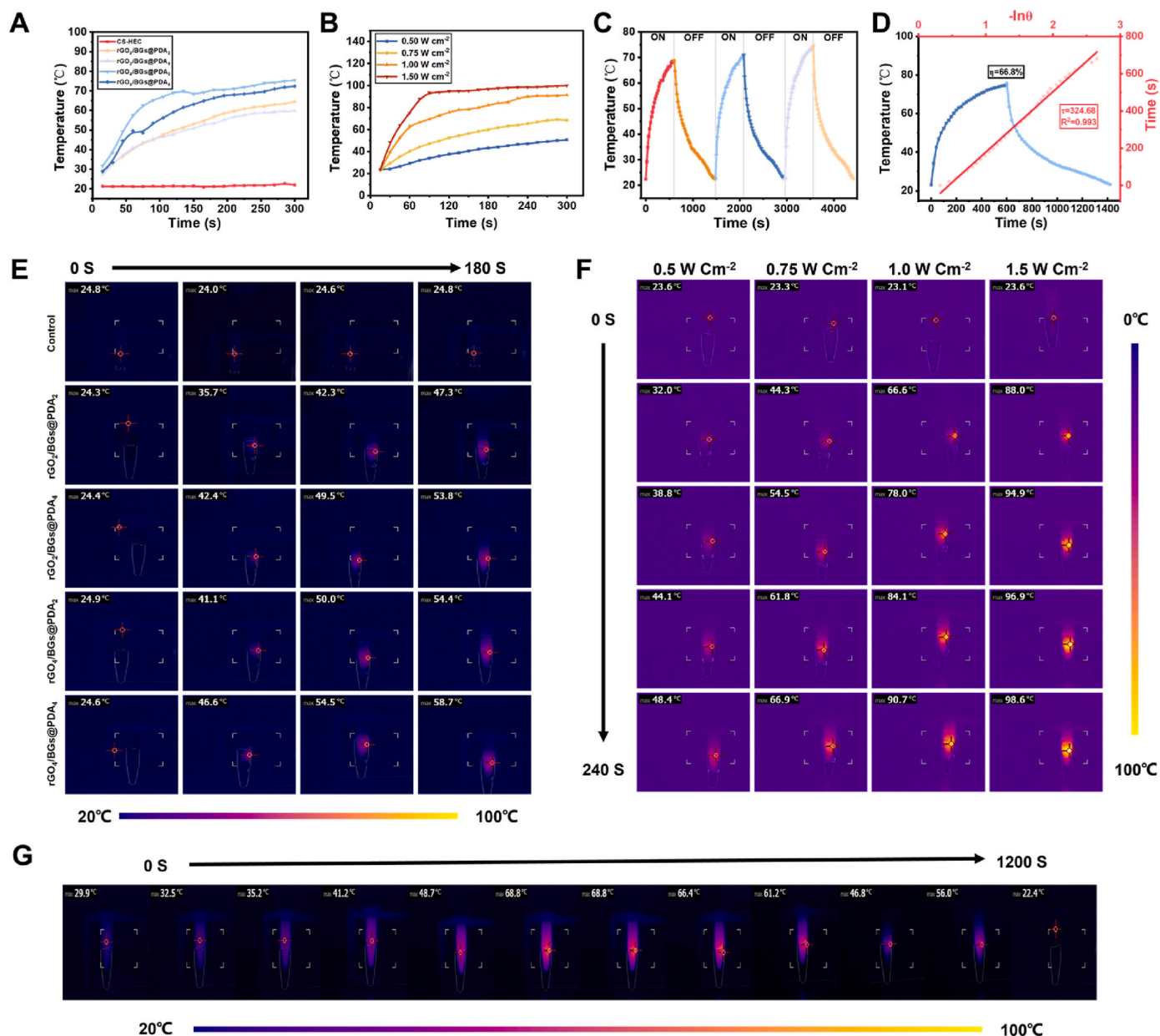
Fig. 4. Photothermal properties of hydrogels. **(A)** Warming curves of different hydrogels at 0.75 W cm^{-2} power. **(B)** Warming curves of rGO$_2$/BGs@PDA$_4$ hydrogel under different powers irradiation. **(C)** Warming and cooling curves of rGO$_2$/BGs@PDA$_4$ hydrogel with three consecutive on/off cycles of laser irradiation. **(D)** Photothermal conversion efficiency of hydrogels containing rGO$_2$/BGs@PDA$_4$. **(E)** Graphs of the effect of warming different hydrogels at 0.75 W cm^{-2} power. **(F)** Graphs of warming effect of rGO$_2$/BGs@PDA$_4$ hydrogel under different powers irradiation. **(G)** Graphs of the effect of rGO$_2$/BGs@PDA$_4$ hydrogel with one on/off cycle of laser irradiation.

hydrogel was comparatively weaker, likely due to reduced cross-linking within the hydrogel. The swelling behavior of rGO$_2$/BGs@PDA$_2$ and rGO$_4$/BGs@PDA$_2$ hydrogels was similar, which may be attributed to the redox reaction between rGO and PDA, potentially decreasing the likelihood of chemical bond formation between rGO and water molecules. However, when the ratio of BGs@PDA was increased in the rGO$_2$/BGs@PDA$_4$ and rGO$_4$/BGs@PDA$_4$ hydrogels, the swelling properties were significantly improved, surpassing those of the first three groups. This result suggested that the swelling characteristics of hydrogels can be effectively regulated to optimize their performance for specific applications by adjusting the ratio of BGs@PDA. The stability of the hydrogels is of critical importance to ensure a stable release of the drug and to maintain the morphology of the hydrogel during the healing process. As shown in Fig. 3H, the synthesized hydrogels first reached the solvation equilibrium and maintained the steady state for a certain

period, and then gradually underwent degradation. CS-HEC exhibited a shorter maintenance duration and accelerated degradation, while rGO$_2$/BGs@PDA$_4$ and rGO$_4$/BGs@PDA$_4$ hydrogels demonstrated prolonged maintenance and slower degradation. This behavior is likely due to the introduction of rGO, which enhanced the cross-linking density, and PDA, which promotes chemical cross-linking with water molecules and CS.

The gradual degradation of the hydrogel during wound healing protects the wound from external disturbances and facilitates the controlled release of therapeutic agents, which is critical for the development of wound dressings. An enzyme that degrades polymers, lysozyme, is ubiquitously found in human plasma and serum and is particularly abundant in wound exudate. It is widely used to assess the biodegradability of hydrogels [64]. PBS with lysozyme was used for the degradation of CS-HEC, rGO$_2$/BGs@PDA$_4$, rGO$_2$/BGs@PDA$_4$, and
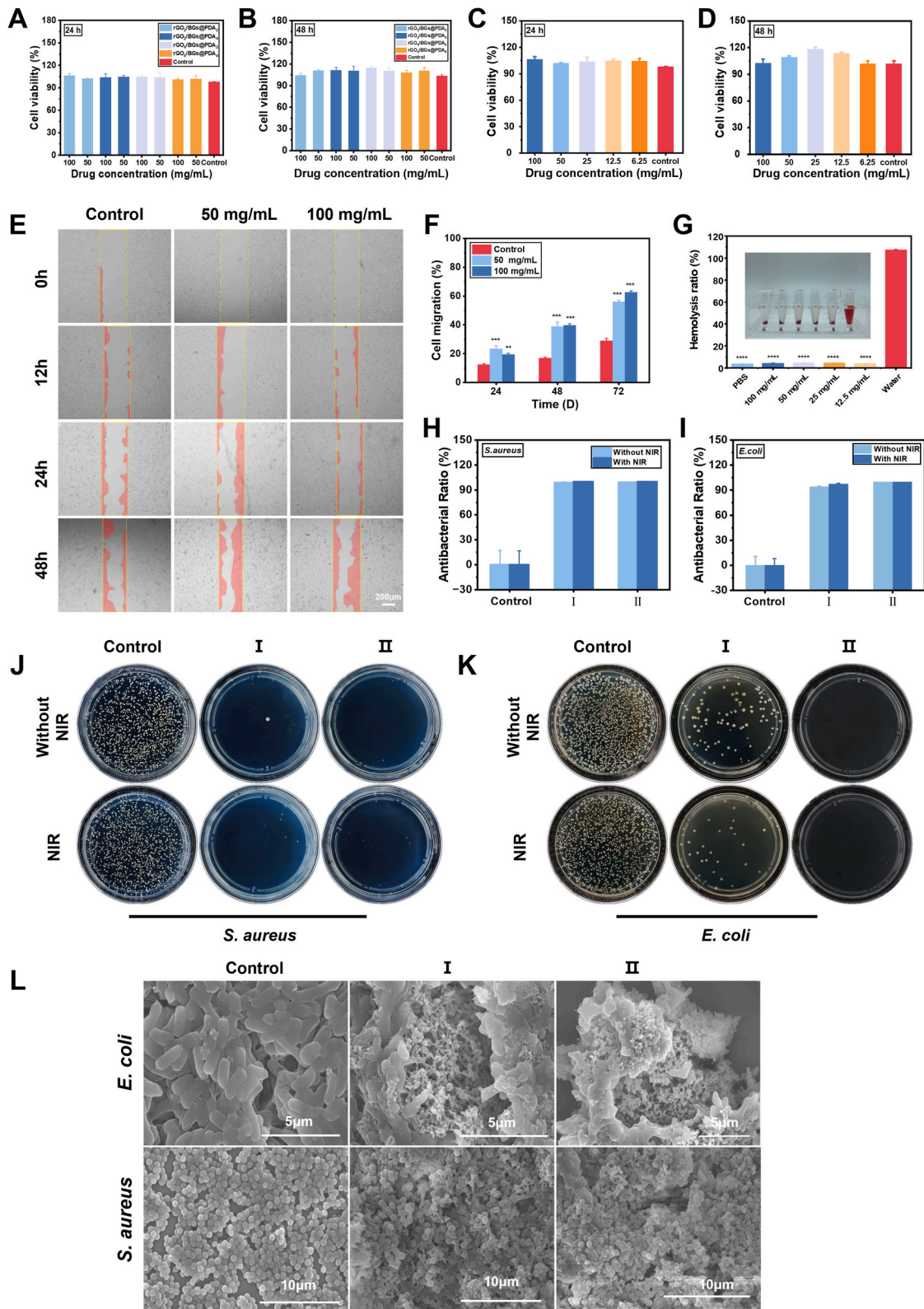
Fig. 5. Biocompatibility and hemolysis assays and *in vitro* antimicrobial assays. **(A) and (B)** Cell viability assessments with hydrogel extract at different concentrations of 100 mg/mL and 50 mg/mL, respectively. **(C) and (D)** CCK-8 assay of rGO$_2$/BGs@PDA$_4$ hydrogel extracts at different concentrations. **(E)** Wound healing assay of rGO$_2$/BGs@PDA$_4$ hydrogel at concentrations of 100 mg/mL and 50 mg/mL. **(F)** Cell migration rate in the wound healing assay. **(G)** Hemolysis assay and hemolysis rate of rGO$_2$/BGs@PDA$_4$ hydrogel extracts of different concentrations. Insert the corresponding picture of the hemolysis experiment. **(H) and (I)** Bacterial viability of *S. aureus* and *E. coli* co-cultured with PBS (Control), AgNCs contained hydrogels (Group I), AgNCs and rGO$_2$/BGs@PDA$_4$ contained hydrogels (Group II), with and without light exposure. **(J) and (K)** Corresponding colony-forming unit (CFU) assay results for figure H and I. **(L)** Scanning electron microscopy (SEM) images of *S. aureus* and *E. coli* after different treatments, scale bars at 5 μm and 10 μm *P < 0.05, **P < 0.01, ***P < 0.001.

rGO$_2$/BGs@PDA$_4$ hydrogels. As illustrated in Fig. 3I, the rate at which the CS-HEC hydrogel degrades was more rapid compared to the other materials, which can be ascribed to its intrinsic physical cross-linking mechanisms, including hydrogen bonding and van der Waals forces. In contrast, the other hydrogels not only featured these physical cross-links but also incorporated chemical cross-links, such as Schiff bases. Furthermore, as the content of BGs@PDA and rGO increased, the degradation period was extended, likely due to enhanced chemical cross-linking and increased overall cross-linking density within the hydrogels.

In wound infection, bacterial attack triggers the overproduction of free radicals, prolonging inflammation and hindering the healing process [65]. Consequently, the capacity of hydrogels to scavenge free radicals is essential for enhancing the healing of wounds. To assess the free radical scavenging capacity of the hydrogels, the DPPH antioxidant assay was conducted. The free radical scavenging rate of CS-HEC hydrogel was 25.60 ± 1.76 %. In comparison, the other hydrogels showed superior antioxidant properties with scavenging rates of 58.70 ± 1.14 % (rGO$_2$/BGs@PDA$_2$), 63.06 ± 1.50 % (rGO$_2$/BGs@PDA$_4$), 71.54 ± 0.81 % (rGO$_4$/BGs@PDA$_2$) and 73.05 ± 0.84 % (rGO$_4$/Gs@PDA$_4$), respectively (Fig. 3J). This enhancement may be attributed to the introduction of rGO and PDA, which enhance antioxidant capacity; rGO offers increased interaction opportunities with free radicals due to its oxygen-containing functional groups and large surface area, while the abundant phenolic -OH groups in PDA act as effective electron donors, facilitating reactions with and neutralizing free radicals.

Conductive wound dressings facilitate healing by mimicking endogenous electrical currents in the skin, effectively promoting the aggregation of key cells such as neutrophils, macrophages, and keratinizing cells at the wound site [12,66,67]. GO is rich in oxygen and features various functional groups, including hydroxyl, epoxy, and carboxyl groups. These oxygen-containing groups make GO highly dispersible and relatively hydrophilic but significantly reduce its electrical conductivity. The rGO restores part of its conjugated structure and improves electrical conductivity, although the process is incomplete, and some residual oxygen functional groups remain. Despite this, the electrical conductivity of rGO is significantly higher than that of pristine GO [62]. Therefore, it was chosen as the conductive component to impart electrical conductivity to the hydrogel. As shown in Fig. 3K, the conductivity of the hydrogel was significantly enhanced with the increase of rGO content, and the conductivity of CS-HEC hydrogel was 9.59 ± 0.19 %. The electrical conductivities of GO$_2$/BGs@PDA$_2$, rGO$_2$/BGs@PDA$_4$, rGO$_4$/BGs@PDA$_2$, and rGO$_4$/BGs@PDA$_4$ were all enhanced significantly, which were 60.78 ± 15.10 %, 64.20 ± 0.95 %, 83.29 ± 0.21 %, 88.06 ± 0.63 %, respectively. These results align with the previous study that an increase in rGO content significantly enhances the conductivity of the hydrogels.

3.4. Photothermal property

To assess the impact of rGO on photothermal conversion efficiency, BGs@PDA hydrogels were compared to rGO$_2$/BGs@PDA$_4$ hydrogels under identical laser irradiation conditions. The result, shown in Fig. S5, indicated that rGO-containing hydrogels demonstrated significantly higher photothermal conversion efficiencies, confirming rGO's positive influence on the photothermal properties of hydrogel materials. Furthermore, the UV–vis absorption spectral analysis of the rGO$_2$/BGs@PDA$_4$ hydrogel revealed a significant absorption capacity in the near-infrared (NIR) region (Fig. S6), suggesting its potential applications as a photothermal conversion material. The temperature changes of the rGO/BGs@PDA hydrogel during and after exposure to an 808 nm laser for 6 min, as well as it cools down to room temperature, owed in Fig. 4D. For further analysis, we plotted the relationship between time during the cooling process and the negative natural logarithm of the driving force temperature (Fig. 4D). According to relevant study [68], the

photothermal conversion efficiency of the hydrogel was determined to be as high as 66.8 % through precise calculations, which significantly demonstrates its potential application in the field of photothermal therapy.

The photothermal conversion efficiency of various hydrogels at a constant power of 0.75 W cm^{-2} is illustrated in Fig. 4A and E. Under 808 nm laser irradiation, the temperature rise accelerated with increased rGO content. After 150s irradiation, the internal temperature of hydrogels can reach 21.4 °C (CS-HEC), 50.8 °C (rGO$_2$/BGs@PDA$_2$), 53 °C (rGO$_2$/BGs@PDA$_4$), 63.1 °C (rGO$_4$/BGs@PDA$_2$), 68.3 °C(rGO$_4$/BGs@PDA$_4$), respectively. When PTT is employed to eliminate bacteria at the wound site, the temperature of dressings should not exceed 50 °C or it will cause irreversible damage to the wound tissue [69,70]. To ensure safe and effective PTT, it is important to regulate the photothermal properties by adjusting the rGO content. The rGO$_2$/BGs@PDA$_4$ hydrogel demonstrated optimal photothermal efficiency for this purpose.

Subsequently, the photothermal conversion efficiencies of rGO$_2$/BGs@PDA$_4$ hydrogel at different power levels were explored, specifically at 0.5 W cm^{-2}, 0.75 W cm^{-2}, 1.0 W cm^{-2}, and 1.5 W cm^{-2}. The findings illustrated in Fig. 4B and F indicate that the temperature increase of the hydrogel exhibited a clear upward trend as the laser power increased. After the irradiation time of 120 s, the corresponding temperatures reached 30.8 °C, 43.7 °C, 44.1 °C, and 50.7 °C, respectively. Considering that excessive temperature may cause damage to the wound tissue in practical applications, we adopted a power level of 0.75 W cm^{-2} in the following experiments to ensure the safety and efficacy of PTT. This decision was based on a rigorous analysis and an assessment of the requirements of clinical applications, aiming to establish a performance parameter that is both safe and effective for subsequent antimicrobial and animal testing. Finally, we investigated the photothermal stability of the rGO$_2$/BGs@PDA$_4$ hydrogel by irradiating it with three consecutive on/off cycles of laser irradiation. After three cycles of irradiation, the hydrogel exhibited exceptional photothermal stability with its temperature change (ΔT) consistently maintained at a stable level of 40 °C, indicating the reliability and robustness of the rGO$_2$/BGs@PDA$_4$ hydrogel under repeated photothermal stimulation (Fig. 4C and G).

3.5. Biocompatibility of hydrogels

The biocompatibility of hydrogels is a key consideration when evaluating their potential application as wound dressings. For this purpose, cytotoxicity tests, live/dead cell staining analysis, cell scratch assays, and blood compatibility tests were applied to evaluate the biosafety of hydrogels. Firstly, the CCK-8 method was employed to assess the impact of hydrogel extracts on cell viability. Extracts from various hydrogels were co-cultured with cells for 24 and 48 h, resulting in cell viability above 85 % for both periods, which was significantly higher than that of the control group, thereby demonstrating established biocompatibility (Fig. 5A and B). Building on insights from earlier photothermal studies, rGO$_2$/BGs@PDA$_4$ hydrogel was chosen for detailed examination. As depicted in Fig. 5C and D, after co-culturing different concentrations of hydrogel extracts with cells, the cell viability remained over 85 % for all tested concentrations. Notably, after 24 and 48 h, extracts at 100 mg/mL and 50 mg/mL concentration significantly enhanced cell proliferation compared to other groups as well as the control. These results not only reaffirmed the biocompatibility of rGO$_2$/BGs@PDA$_4$ hydrogel but also highlighted its positive influence on cell proliferation at specific concentrations. To further validate the biosafety and effect of rGO$_2$/BGs@PDA$_4$ hydrogel on cell proliferation, a live/dead cell staining analysis was performed. As shown in Fig. S7, co-culturing different concentrations of hydrogel extracts with cells for 24 h did not lead to significant cell death and showed a pro-proliferative effect at concentrations of 100 mg/mL, 50 mg/mL, 25 mg/mL, and 12.5 mg/mL. These results indicate that the hydrogel is
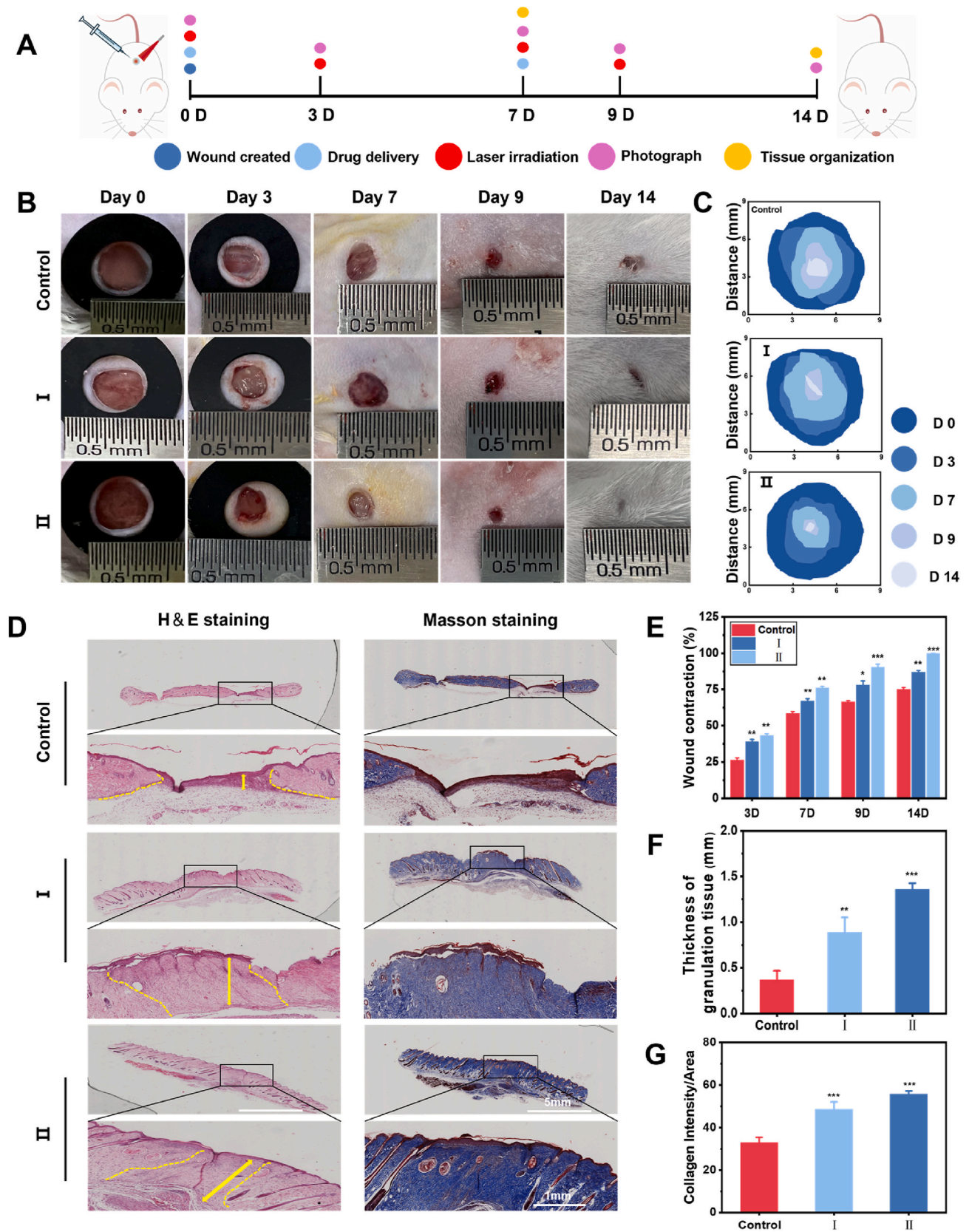
Fig. 6. Hydrogel *in vivo* wound healing effect. **(A)** Wound healing effect of 3M commercial film as control group, rGO$_2$/BGs@PD$_4$ hydrogel as group I, rGO$_2$/BGs@PD$_4$ hydrogel with light treatment as group II at 0, 3, 7, 9, and 14 days (n = 6). **(B)** Wound healing schematic diagrams corresponding to the control group, group I, and group II. **(C)** Wound healing rate statistics at different healing times. **(D)** HE and Masson staining of wound tissue after 14 days, and its local magnification, scale bar 5 mm and 1 mm. **(E)** Statistics of granulation tissue thickness in the control group, group I and group II. **(F)** Collagen-positive area in control group, group I and group II. *P < 05, **P < 0.01, ***P < 0.01, ***P < 0.001.

biocompatible and promotes short-term cell proliferation. At 48 h, the pro-proliferative effect of the hydrogel was significantly superior to that of the control group, although some cell death was observed. This result suggested that the hydrogel retained its pro-proliferative properties over time. Further validation of these pro-proliferative effects was conducted through cell scratch assays. As depicted in Fig. 5E and F, the hydrogel extract at a concentration of 100 mg/mL significantly enhanced cell proliferation and effectively induced cell migration toward the scratched area, surpassing both the control group and the concentration of 50 mg/mL group in efficacy.

To assess the safety of the hydrogel, particularly its blood compatibility as a wound dressing, hemolysis tests were conducted. As shown in Fig. 5G, the hemolysis rate of erythrocytes was less than 5 % (<5 % for good hemocompatibility) for both 100 mg/mL and other concentration groups after incubation with hydrogel extract. This low hemolysis rate suggests that the hydrogel does not induce significant rupture of red blood cells upon contact with the wound, thereby reducing the risk of potential inflammatory reactions and immune rejection.

3.6. In vitro antimicrobial test

The antimicrobial activity of the control and experimental group I (hydrogels containing AgNCs), and experimental group II (hydrogels containing AgNCs and $rGO_2/BGs@PDA_4$) were evaluated using $E.$ $coli$ and $S.$ $aureus$. As shown in Fig. 5J and K, plate counting results indicated that the control group exhibited excessive bacterial growth both with and without laser irradiation, suggesting that NIR irradiation alone had minimal impact on bacterial proliferation. As shown in Fig. 5H and I, compared to the control group, the experimental results indicate that after co-culturing with $Staphylococcus$ $aureus$, the antibacterial rates of experimental group I reached 98.2 % and 100 % under non-illuminated and illuminated conditions, respectively, while experimental group II exhibited antibacterial rates of 99.2 % and 100 % under the same conditions. In the co-culturing experiment with $Escherichia$ $coli$, the antibacterial rates of experimental group I were 94.3 % and 97.5 % under non-illuminated and illuminated conditions, respectively, whereas experimental group II showed antibacterial rates close to 100 % regardless of illumination. These results demonstrated that the proposed hydrogel containing AgNCs and $rGO_2/BGs@PDA_4$ achieved rapid antibacterial capability and sustained antibacterial effect by PPT and Ag ion mediated synergistic effect. These results confirm that CS-HEC hydrogels delivered with $rGO_2/BGs@PDA_4$ can utilize PTT and AgNCs for synergistic antimicrobial capacity.

Specifically, the introduction of $rGO_2/BGs@PDA_4$ in the hydrogel significantly enhanced its photothermal conversion efficiency, thereby further increasing the temperature and enabling rapid and efficient sterilization in the early stages. The plate count experiments demonstrated that $rGO_2/BGs@PDA_4$ hydrogels exhibited excellent antibacterial properties regardless of whether they were exposed to light or not. This phenomenon may be attributed to the antibacterial properties of both rGO and BGs@PDA. Additionally, the photothermal experiments revealed that $rGO_2/BGs@PDA_4$ possesses outstanding photothermal conversion efficiency, which further enhanced the antibacterial performance of the hydrogel. After laser irradiation in the early stages, the hydrogel could rapidly kill the majority of bacteria, thereby reducing the need for AgNCs in the later stages of sterilization.

The addition of AgNCs alone in the hydrogel primarily played a role in slow sterilization in the later stages. Plate count experiments showed that after co-culturing with bacteria, AgNCs slowly released and met bacteria, leading to bacterial death. The experiments also revealed that hydrogels containing only AgNCs exhibited a high inhibition rate even when co-cultured with $S.$ $aureus$ without light exposure. When co-cultured with $E.$ $coli$, the AgNCs hydrogel demonstrated a significant inhibitory effect compared to the PBS group, and this inhibition was even more pronounced after light exposure. It is speculated that this is related to the fact that AgNCs can also serve as a photothermal agent in

photothermal therapy, further enhancing their antibacterial effect.

The antibacterial activities of the control, group I, and II hydrogels were further evaluated using live/dead bacterial staining assays. As shown in Fig. S8 (A) and (B), dead bacterial (red fluorescence) was detected rarely in the PBS group, irrespective of NIR laser irradiation. Unlike the control group, both group I and group II exhibited a notable decrease in green fluorescence intensity and an increase in red fluorescence intensity, with these effects becoming more evident after irradiation.

The morphological changes in $E.$ $coli$ and $S.$ $aureus$ treated with the control, group I, and group II hydrogels were further observed. As shown in Fig. 5L, bacteria in the control group maintained a smooth and intact surface with no significant morphological changes even after laser irradiation, indicating negligible damage following NIR treatment. In contrast, bacteria incubated with hydrogel group I exhibited slight wrinkling or collapse on their surfaces. Further examination of hydrogel group II revealed more pronounced morphological alterations in $E.$ $coli$ and $S.$ $aureus$, including significant rupture or shrinkage, due to its unique synergistic antibacterial mechanism involving PTT and AgNCs permeation. By carefully comparing the results of experimental group I and experimental group II, we can clearly observe that the combined application of PTT and AgNCs has demonstrated a significant synergistic antibacterial effect. This synergistic action not only enhances the antibacterial efficiency but also exhibits superior therapeutic efficacy in practical applications, further validating the complementary and synergistic nature of PTT and AgNCs in antibacterial treatment. These findings highlight the potential advantages of the proposed hydrogel in antibacterial applications.

3.7. In vivo wound healing assessment

The efficacy of the rGO/BGs@PDA hydrogel dressing in promoting wound healing was evaluated by using full-thickness skin (Fig. 6A). Considering the mechanical properties, biocompatibility, and photothermal conversion efficiency of the hydrogel, the $rGO_2/BGs@PD_4$ hydrogel was chosen as the experimental group I, while the light-treated version was group II, with 3M commercial film as the control. From day 0 to day 14, wound photography showed a gradual decrease in wound area across all groups (Fig. 6B, C and E). Notably, groups I and II exhibited significantly enhanced wound healing rates from day three onward (P < 0.001), indicating that the $rGO_2/BGs@PD_4$ hydrogel significantly accelerated the healing process. By day 14, group II wounds were nearly healed, with neoplastic hairs covering the surface. The healing rates on day 14 were 87.03 ± 0.99 % for group I, 75.02 ± 1.29 % for the control, and an impressive 99.9 ± 0.1 % for group II, demonstrating the superior efficacy of the $rGO_2/BGs@PD_4$ hydrogel, particularly with light treatment. The enhanced healing effect is likely attributed to the $rGO_2/BGs@PD_4$ hydrogel's ability to facilitate a controlled degradation process during wound repair. Within this hydrogel matrix, the BGs are encapsulated by PDA, which provides a degradation environment that slowly releases encapsulated ions such as Si^{2+} and Ca^{2+}. These ions, in turn, stimulate the secretion of various cytokines, including growth factors, at the wound site. This promotes accelerated healing, particularly after the initial observation period, which further enhances the degradation of BGs. Additionally, AgNCs encapsulated within the hydrogel are released gradually as the hydrogel degrades. Given their small particle size and the results of biocompatibility tests, the potential cytotoxicity of AgNCs is negligible in the context of wound healing promotion. This suggests that the $rGO_2/BGs@PD_4$ hydrogel offers a promising strategy for accelerated wound repair with minimal cytotoxic concerns.

On day 14, tissue from the wound sites of the mice was collected and evaluated for healing effects among the groups using HE and Masson staining. As illustrated in Fig. 6D, an assessment of inflammation in the initial phases of healing demonstrated that the inflammatory responses observed in groups I and II were notably reduced compared to those in
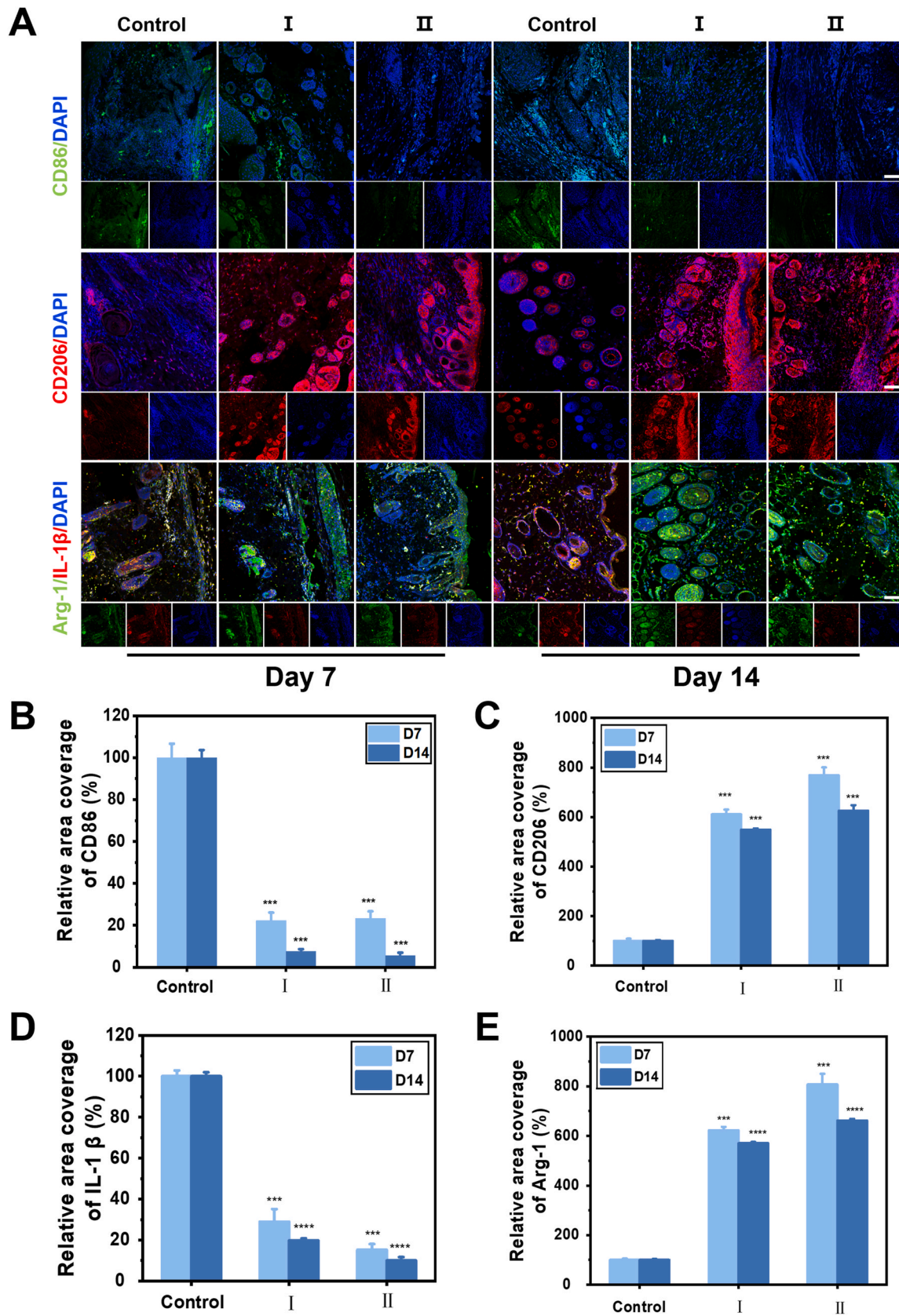
Fig. 7. Immunofluorescence analysis. **(A)** Immunofluorescence of CD206, CD86, Arg-1, and IL-1β-labeled wound tissue on day 7 and 14, scale bar 200 μm. **(B)** CD86 **(C)** CD206 **(D)** IL-1β **(E)** Arg-1 relative percent area coverage statistics. For all data, controls were set at 100 %. *P < 0.05, **P < 0.01, ***P < 0.001.

the control group. This suggested that the $rGO_2/BGs@PD_4$ hydrogels were effective in diminishing inflammation, thus fostering a more favorable environment for the healing of wounds. During the ongoing inflammation, granulation tissue proliferates to dissolve and absorb necrotic tissue and foreign matter, filling the gaps and accelerating wound healing [12,71]. Consequently, the measurement of granulation tissue thickness serves as a key parameter in assessing wound healing. As illustrated in Fig. 6D and F, when evaluating the HE stained granulation tissue from the control group, as well as Groups I and II on the 14th day, it is evident that the granulation tissue in Group II exhibits a notable increase in thickness compared to the other two groups. This phenomenon may be due to the combined effects of temperature increase after illumination, acting in two aspects. Firstly, the rise in temperature effectively kills bacteria in the wound area, significantly reducing the level of inflammation and the risk of bacterial infection. Secondly, the increased temperature also accelerates the degradation of bioactive glass, releasing more bioactive components that can expedite the healing process of the wound, providing a more favorable environment for cell proliferation and neovascularization, thus promoting rapid healing and repair. The synergistic action of this series of reactions offers robust support and assurance for wound healing.

The buildup of collagen at the injury site plays an essential role in scar contraction, the regeneration of epithelial tissue, and the early development of the dermis [72,73]. Evaluations of collagen remodeling in the wound healing area after fourteen days were conducted using Masson staining, which indicated the collagen in group II was thicker, denser, and more orderly arranged compared to the other two groups (Fig. 6D and G). The collagen level in group II was measured at 55.73 ± 1.46 %, showing a notable increase compared to group I and the control group, which had values of 48.54 ± 3.46 % and 32.96 ± 2.40 %, respectively. These findings confirm that the $rGO_2/BGs@PD_4$ hydrogel, particularly with light exposure, enhances wound healing capabilities. It is postulated that the occurrence of this phenomenon may be associated with the increase in wound temperature following illumination, as the rise in temperature can lead to the death of most bacteria, thereby significantly reducing the inflammatory response. This change in the environment creates favorable conditions for the accumulation of collagen, which in turn facilitates the smooth progression of the wound healing process.

3.8. Immunofluorescence analysis

To further evaluate inflammation at the wound healing site, we analyzed the cytokines IL-1β and Arg-1, as well as the macrophage surface markers CD86 and CD206 by immunofluorescence staining. As shown in Fig. 7A, both on days 7 and 14, the levels of CD86 and IL-1β proteins were significantly reduced in the hydrogel groups, especially in the light-treated hydrogel group, compared to the control group. Conversely, the levels of CD206 and Arg-1 proteins were significantly increased. These findings indicate that the hydrogel, particularly when treated with light, effectively modulated the immune response, reduced inflammation, and promoted the formation of an anti-inflammatory environment. On day 7, fluorescence intensities of IL-1β and CD86, which indicate inflammatory responses, were significantly lower in groups I and II compared to the control group (Fig. 7B and C). In contrast, the fluorescence intensities of Arg-1 and CD206 (anti-inflammatory indicators) were significantly increased, suggesting that the $rGO_2/BGs@PD_4$ hydrogel also positively promotes anti-inflammatory responses and contributes to wound healing (Fig. 7D and E). By day 14, these differences were even more pronounced, further confirming the superiority of our experimental groups I and II in attenuating wound inflammatory responses and promoting anti-inflammatory responses. These results fully validate our hypothesis that the $rGO_2/BGs@PD_4$ hydrogel not only effectively reduces the inflammatory response of wounds, but also actively promotes the anti-inflammatory process, thereby accelerating wound healing.

4. Conclusion

In the healing process of infected wounds, urgent challenges are posed by the overuse of antibiotics leading to resistance and the cytotoxicity resulting from the extensive use of metal ions that need to be addressed. A thermally stable injectable hydrogel is presented in this study, which integrates PTT with AgNCs to achieve a synergistic antibacterial effect. The rGO in the hydrogel is utilized as a photothermal agent, allowing light energy to be rapidly converted into heat upon irradiation, thereby elevating the temperature of the hydrogel and effectively killing bacteria. Compared to other metal ion-based antibacterial hydrogels, a lower dosage of metal ions can be employed using AgNCs after an extensive bacterial killing through PTT, facilitating long-term treatment and preventing bacterial reinfection. The effectiveness of this synergistic antibacterial action is confirmed by bacterial viability/dead staining and SEM observations. Moreover, the homogeneity of rGO in aqueous solutions allows it to be incorporated with BGs@PDA via redox reactions, thus resolving the issue of BGs@PDA precipitating at the bottom before the hydrogel gels. Additionally, exudates are continuously absorbed by the hydrogel during the wound-healing process, and the slow degradation of bioactive glass is addressed by the encapsulation of PDA. During degradation, various ions, including Si^{2+}, Ca^{2+}, and Na^+, are released by bioactive glass, which facilitates the release of multiple biofactors, such as fibroblast growth factor and basic epidermal growth factor, thereby accelerating wound healing. Furthermore, the electrical conductivity and free radical scavenging ability of the hydrogel are significantly enhanced by rGO generated from redox reactions, an advantage not possessed by GO. The hydrogel, composed of CS and HEC, is improved in mechanical strength and self-healing capacity through the utilization of abundant functional groups on PDA and rGO for chemical and physical cross-linking. Excellent biocompatibility is demonstrated by this hydrogel in cell experiments, and significant promotion of cell proliferation and migration is observed. Upon application to wounds, inflammation is effectively inhibited by the hydrogel, collagen deposition is accelerated, and further promotion of wound healing is achieved. These findings underscore the potential of this hydrogel in wound repair and lay a solid foundation for future clinical applications. In summary, the combination of PTT and the synergistic antibacterial action of AgNCs positions this multifunctional hydrogel as a promising therapeutic option for clinical applications.

CRediT authorship contribution statement

Fuqiang Song: Writing – review & editing, Writing – original draft, Visualization, Validation, Project administration, Methodology, Investigation, Formal analysis, Data curation, Conceptualization. **Anqi Ye:** Writing – review & editing, Methodology, Formal analysis, Data curation, Conceptualization. **Linyuan Jiang:** Methodology, Formal analysis, Data curation. **Yang Lu:** Methodology, Formal analysis, Data curation. **Yanzhen Feng:** Formal analysis, Data curation. **Rong Huang:** Formal analysis, Data curation. **Siting Du:** Formal analysis, Data curation. **Xiaoyu Dong:** Methodology, Formal analysis, Data curation, Conceptualization. **Ting Huang:** Formal analysis, Data curation. **Ping Li:** Formal analysis, Data curation. **Liangliang Yang:** Formal analysis, Data curation. **Jinjing Zhang:** Resources, Formal analysis, Data curation. **Mengjia Xu:** Writing – review & editing, Visualization, Validation, Supervision, Resources, Project administration, Methodology, Investigation, Funding acquisition. **Li Cheng:** Writing – review & editing, Supervision, Resources, Investigation, Funding acquisition. **Jian Xiao:** Writing – review & editing, Visualization, Validation, Supervision, Resources, Project administration, Methodology, Investigation, Funding acquisition.

Declaration of competing interest

The authors declare that they have no known conflict of interest that

could have appeared to influence the work reported in this paper.

Appendix A. Supplementary data

Supplementary data to this article can be found online at https://doi.org/10.1016/j.mtbio.2024.101439.

Data availability

Data will be made available on request.

References

[1] D. Chouhan, N. Dey, N. Bhardwaj, B.B. Mandal, Emerging and innovative approaches for wound healing and skin regeneration: current status and advances, Biomaterials 216 (2019) 119267, https://doi.org/10.1016/j.biomaterials.2019.119267.

[2] M. Hosseini, A. Shafiee, Engineering bioactive scaffolds for skin regeneration, Small 17 (41) (2021) 2101384, https://doi.org/10.1002/smll.202101384.

[3] Y.P. Liang, J.H. He, B.L. Guo, Functional hydrogels as wound dressing to enhance wound healing, ACS Nano 15 (8) (2021) 12687–12722, https://doi.org/10.1021/acsnano.1c04206.

[4] S. Zhang, G. Ge, Y. Qin, W. Li, J. Dong, J. Mei, R. Ma, X. Zhang, J. Bai, C. Zhu, W. Zhang, D. Geng, Recent advances in responsive hydrogels for diabetic wound healing, Materials Today Bio 18 (2023), https://doi.org/10.1016/j.mtbio.2022.100508.

[5] Y.H. He, R.M. Chen, C. Zhao, Q. Lu, Z.P. Chen, H.X. Zhu, Q. Bu, L. Wang, H. He, Design of near-infrared-triggered cellulose nanocrystal-based intelligent wound dressings for drug-resistant bacteria-infected wound healing, ACS Appl. Mater. Interfaces 14 (46) (2022) 51630–51644, https://doi.org/10.1021/acsami.2c13203.

[6] S. Tomar, R. Pandey, P. Surya, R. Verma, R. Mathur, G. Gangenahalli, S. Singh, Multifunctional, adhesive, and PDA-coated bioactive glass reinforced composite hydrogel for regenerative wound healing, ACS Biomater. Sci. Eng. 9 (3) (2023) 1520–1540, https://doi.org/10.1021/acsbiomaterials.2c01223.

[7] N. Namviriyachote, V. Lipipun, Y. Akkhawattanangkul, P. Charoonrut, G.C. Ritthidej, Development of polyurethane foam dressing containing silver and asiaticoside for healing of dermal wound, Asian J. Pharm. Sci. 14 (1) (2019) 63–77, https://doi.org/10.1016/j.ajps.2018.09.001.

[8] S. Homaeigohar, A.R. Boccaccini, Antibacterial biohybrid nanofibers for wound dressings, Acta Biomater. 107 (2020) 25–49, https://doi.org/10.1016/j.actbio.2020.02.022.

[9] S. Jiang, B.C. Ma, W. Huang, A. Kaltbeitzel, G. Kizisavas, D. Crespy, K.A.I. Zhang, K. Landfester, Visible light active nanofibrous membrane for antibacterial wound dressing, Nanoscale Horiz 3 (4) (2018) 439–446, https://doi.org/10.1039/c8nh00021b.

[10] J. Li, X. Sun, J. Dai, J. Yang, L. Li, Z. Zhang, J. Guo, S. Bai, Y. Zheng, X. Shi, Biomimetic multifunctional hybrid sponge via enzymatic cross-linking to accelerate infected burn wound healing, Int. J. Biol. Macromol. 225 (2023) 90–102, https://doi.org/10.1016/j.ijbiomac.2022.12.024.

[11] L. Li, D.F. Chen, J.L. Chen, C. Yang, Y.Y. Zeng, T. Jin, Y.M. Zhang, X.Y. Sun, H.L. Mao, Z.X. Mu, X.K. Shen, Z.W. Ruan, X.J. Cai, Gelatin and catechol-modified quaternary chitosan cotton dressings with rapid hemostasis and high-efficiency antimicrobial capacity to manage severe bleeding wounds, Mater. Des. 229 (2023), https://doi.org/10.1016/j.matdes.2023.111927.

[12] L.P. Qiao, Y.P. Liang, J.Y. Chen, Y. Huang, S.A. Alsareii, A.M. Alamri, F.A. Harraz, B.L. Guo, Antibacterial conductive self-healing hydrogel wound dressing with dual dynamic bonds promotes infected wound healing, Bioact. Mater. 30 (2023) 129–141, https://doi.org/10.1016/j.bioactmat.2023.07.015.

[13] Y.K. Ren, S.S. Ma, D. Zhang, S. Guo, R. Chang, Y.M. He, M.H. Yao, F.X. Guan, Functionalized injectable hyaluronic acid hydrogel with antioxidative and photothermal antibacterial activity for infected wound healing, Int. J. Biol. Macromol. 210 (2022) 218–232, https://doi.org/10.1016/j.ijbiomac.2022.05.024.

[14] C. Gao, W. Dai, X. Wang, L. Zhang, Y. Wang, Y. Huang, Z. Yuan, X. Zhang, Y. Yu, X. Yang, Q. Cai, Magnesium gradient-based hierarchical scaffold for dual-lineage regeneration of osteochondral defect, Adv. Funct. Mater. 33 (43) (2023), https://doi.org/10.1002/adfm.202304829.

[15] Y.M. Fan, M. Lüchow, Y.N. Zhang, J.J. Lin, L. Fortuin, S. Mohanty, A. Brauner, M. Malkoch, Nanogel encapsulated hydrogels as advanced wound dressings for the controlled delivery of antibiotics, Adv. Funct. Mater. 31 (7) (2021) 2006453, https://doi.org/10.1002/adfm.202006453.

[16] X.G. Yang, D.D. Guo, X.T. Ji, C.Y. Shi, J.M. Messina, L.Y. Suo, J.T. Luo, Telodendrimer functionalized hydrogel platform for sustained antibiotics release in infection control, Acta Biomater. 178 (2024) 147–159, https://doi.org/10.1016/j.actbio.2024.02.041.

[17] Y. Chen, Y.J. Gao, Y. Chen, L. Liu, A.C. Mo, Q. Peng, Nanomaterials-based photothermal therapy and its potentials in antibacterial treatment, J. Contr. Release 328 (2020) 251–262, https://doi.org/10.1016/j.jconrel.2020.08.055.

[18] H. Liu, F. Xing, Y.X. Zhou, P.Y. Yu, J.W. Xu, R. Luo, Z. Xiang, P.M. Rommens, M. Liu, U. Ritz, Nanomaterials-based photothermal therapies for antibacterial applications, Mater. Des. 233 (2023) 112231, https://doi.org/10.1016/j.matdes.2023.112231.

[19] X. Liu, M. Shen, T. Bing, X. Zhang, Y. Li, Q. Cai, X. Yang, Y. Yu, A bioactive injectable hydrogel regulates tumor metastasis and wound healing for melanoma via NIR-light triggered hyperthermia, Adv. Sci. 11 (26) (2024), https://doi.org/10.1002/advs.202402208.

[20] G. Xie, X. Wang, M. Mo, L.B. Zhang, J.T. Zhu, Photothermal hydrogels for promoting infected wound healing, Macromol. Biosci. 23 (2) (2023), https://doi.org/10.1002/mabi.202200378.

[21] Y.L. Xu, H.L. Chen, Y.F. Fang, J. Wu, Hydrogel combined with phototherapy in wound healing, Adv. Healthcare Mater. 11 (16) (2022) 2200494, https://doi.org/10.1002/adhm.202200494.

[22] B.-D. Zheng, M.-T. Xiao, Polysaccharide-based hydrogel with photothermal effect for accelerating wound healing, Carbohydr. Polym. 299 (2023), https://doi.org/10.1016/j.carbpol.2022.120228.

[23] Y. Hu, Q. Zeng, Y. Hu, J. He, H. Wang, C. Deng, D. Li, MXene/zinc ion embedded agar/sodium alginate hydrogel for rapid and efficient sterilization with photothermal and chemical synergetic therapy, Talanta 266 (2024), https://doi.org/10.1016/j.talanta.2023.125101.

[24] H.L. Liu, X.L. Zhu, H.M. Guo, H.L. Huang, S.H. Huang, S.S. Huang, W. Xue, P. Zhu, R. Guo, Nitric oxide released injectable hydrogel combined with synergistic photothermal therapy for antibacterial and accelerated wound healing, Appl. Mater. Today 20 (2020), https://doi.org/10.1016/j.apmt.2020.100781.

[25] Y.K. Zheng, M. Wei, H.B. Wu, F.Y. Li, D.S. Ling, Antibacterial metal nanoclusters, J. Nanobiotechnol. 20 (1) (2022) 328, https://doi.org/10.1186/s12951-022-01538-y.

[26] S. Javani, R. Lorca, A. Latorre, C. Flors, A.L. Cortajarena, A. Somoza, Antibacterial activity of DNA-stabilized silver nanoclusters tuned by oligonucleotide sequence, Acs Appl Mater Inter 8 (16) (2016) 10147–10154, https://doi.org/10.1021/acsami.6b00670.

[27] C. Wang, Y. Huang, Facile preparation of fluorescent Ag-clusters-chitosan-hybrid nanocomposites for bio-applications, New J. Chem. 38 (2) (2014) 657–662, https://doi.org/10.1039/c3nj00951c.

[28] A. Nakal-Chidiac, O. García, L. García-Fernández, F.M. Martín-Saavedra, S. Sánchez-Casanova, C. Escudero-Duch, J. San Román, N. Vilaboa, M.R. Aguilar, Chitosan-stabilized silver nanoclusters with luminescent, photothermal and antibacterial properties, Carbohydr. Polym. 250 (2020), https://doi.org/10.1016/j.carbpol.2020.116973.

[29] M.N. Rahaman, D.E. Day, B.S. Bal, Q. Fu, S.B. Jung, L.F. Bonewald, A.P. Tomsia, Bioactive glass in tissue engineering, Acta Biomater. 7 (6) (2011) 2355–2373, https://doi.org/10.1016/j.actbio.2011.03.016.

[30] C. Yuan, D. Zhang, Y. Tang, Z. Guo, K. Lin, Y. Yu, J. Li, Q. Cai, Fibrous dressing containing bioactive glass with combined chemotherapy and wound healing promotion for post-surgical treatment of melanoma, Biomater. Adv. 149 (2023), https://doi.org/10.1016/j.bioadv.2023.213387.

[31] Y. He, X. Wang, C. Zhang, J. Sun, J. Xu, D. Li, Near-infrared light-mediated cyclodextrin metal–organic frameworks for synergistic antibacterial and anti-biofilm therapies, Small 19 (35) (2023), https://doi.org/10.1002/smll.202300199.

[32] M.K. Yazdi, M. Zare, A. Khodadadi, F. Seidi, S.M. Sajadi, P. Zarrintaj, A. Arefi, M.R. Saeb, M. Mozafari, Polydopamine biomaterials for skin regeneration, ACS Biomater. Sci. Eng. 8 (6) (2022) 2196–2219, https://doi.org/10.1021/acsbiomaterials.1c01436.

[33] L. Duan, H.D. Zhang, M.M. Huang, L. Sang, J.S. Zhang, External mass transfer performance studies in a micropacked bed reactor with Pd/PDA/nickel foam, Ind. Eng. Chem. Res. 63 (28) (2024) 12385–12393, https://doi.org/10.1021/acs.iecr.4c00842.

[34] S. Naseri, W.C. Lepry, S.N. Nazhat, Bioactive glasses in wound healing: hope or hype? J. Mater. Chem. B 5 (31) (2017) 6167–6174, https://doi.org/10.1039/c7tb01221g.

[35] W. Lee, J.U. Lee, B.M. Jung, J.H. Byun, J.W. Yi, S.B. Lee, B.S. Kim, Simultaneous enhancement of mechanical, electrical and thermal properties of graphene oxide paper by embedding dopamine, Carbon 65 (2013) 296–304, https://doi.org/10.1016/j.carbon.2013.08.029.

[36] M. Li, Y.P. Liang, J.H. He, H.L. Zhang, B.L. Guo, Two-pronged strategy of biomechanically active and biochemically multifunctional hydrogel wound dressing to accelerate wound closure and wound healing, Chem. Mater. 32 (23) (2020) 9937–9953, https://doi.org/10.1021/acs.chemmater.0c02823.

[37] Y.B. Schuetz, R. Gurny, O. Jordan, A novel thermoresponsive hydrogel based on chitosan, Eur. J. Pharm. Biopharm. 68 (1) (2008) 19–25, https://doi.org/10.1016/j.ejpb.2007.06.020.

[38] P. Samyn, A platform for functionalization of cellulose, chitin/chitosan, alginate with polydopamine: a review on fundamentals and technical applications, Int. J. Biol. Macromol. 178 (2021) 71–93, https://doi.org/10.1016/j.ijbiomac.2021.02.091.

[39] Y. Luo, L. Cui, L. Zou, Y.P. Zhao, L. Chen, Y. Guan, Y.J. Zhang, Mechanically strong and on-demand dissoluble chitosan hydrogels for wound dressing applications, Carbohydr. Polym. 294 (2022), https://doi.org/10.1016/j.carbpol.2022.119774.

[40] K. Enoch, C.S. Rakavi, A.A. Somasundaram, Thixotropic chitosan hydrogels for biomedical applications: unravelling the effect of chitosan concentration on the mechanical behaviour, Surface. Interfac. 50 (2024) 104475, https://doi.org/10.1016/j.surfin.2024.104475.

[41] A. Noreen, K.M. Zia, S. Tabasum, S. Khalid, R. Shareef, A review on grafting of hydroxyethylcellulose for versatile applications, Int. J. Biol. Macromol. 150 (2020) 289–303, https://doi.org/10.1016/j.ijbiomac.2020.01.265.

[42] I. Hussain, X.F. Ma, L.L. Wu, Z.Y. Luo, Hydroxyethyl cellulose-based electrically conductive, mechanically resistant, strain-sensitive self-healing hydrogels, Cellulose 29 (10) (2022) 5725–5743, https://doi.org/10.1007/s10570-022-04622-6.

[43] T. Fekete, J. Borsa, E. Takács, L. Wojnárovits, Synthesis and characterization of superabsorbent hydrogels based on hydroxyethylcellulose and acrylic acid, Carbohydr. Polym. 166 (2017) 300–308, https://doi.org/10.1016/j.carbpol.2017.02.108.

[44] C. Pan, J.J. Li, W.L. Hou, S.S. Lin, L. Wang, Y. Pang, Y.F. Wang, J.Y. Liu, Polymerization-mediated multifunctionalization of living cells for enhanced cell-based therapy, Adv. Mater. 33 (13) (2021), https://doi.org/10.1002/adma.202007379.

[45] Y.Z. Li, L. Yang, Y. Hou, Z.Z. Zhang, M. Chen, M.X. Wang, J. Liu, J. Wang, Z. H. Zhao, C.M. Xie, X. Lu, Polydopamine-mediated graphene oxide and nanohydroxyapatite-incorporated conductive scaffold with an immunomodulatory ability accelerates periodontal bone regeneration in diabetes, Bioact. Mater. 18 (2022) 213–227, https://doi.org/10.1016/j.bioactmat.2022.03.021.

[46] Y.Y. Dou, Y.W. Zhang, S. Zhang, S. Ma, H. Zhang, Multi-functional conductive hydrogels based on heparin-polydopamine complex reduced graphene oxide for epidermal sensing and chronic wound healing, J. Nanobiotechnol. 21 (1) (2023), https://doi.org/10.1186/s12951-023-02113-9.

[47] G.S. Polymeris, V. Giannoulatou, A. Kyriakidou, I.K. Sfampa, G.S. Theodorou, E. Sahiner, N. Meriç, G. Kitis, K.M. Paraskevopoulos, Bioactivity characterization of 45S5 bioglass using TL, OSL and EPR: comparison with the case of 58S sol-gel bioactive glass, Mater. Sci. Eng., C 70 (2017) 673–680, https://doi.org/10.1016/j.msec.2016.09.051.

[48] J.R. Jones, Review of bioactive glass: from Hench to hybrids, Acta Biomater. 9 (1) (2013) 4457–4486, https://doi.org/10.1016/j.actbio.2012.08.023.

[49] A. Kumar, S. Murugavel, A. Aditya, A.R. Boccaccini, Mesoporous 45S5 bioactive glass: synthesis, dissolution and biomineralization behavior, J. Mater. Chem. B 5 (44) (2017) 8786–8798, https://doi.org/10.1039/c7tb01738c.

[50] K. Sahoo, T.R. Gazi, S. Roy, I. Chakraborty, Nanohybrids of atomically precise metal nanoclusters, Commun. Chem. 6 (1) (2023) 157, https://doi.org/10.1038/s42004-023-00958-7.

[51] X.Z. Luo, S.W. Cheng, W. Zhang, K. Dou, R. Wang, F.B. Yu, Near-infrared fluorescence probe for indication of the pathological stages of wound healing process and its clinical application, ACS Sens. 9 (2) (2024) 810–819, https://doi.org/10.1021/acssensors.3c02147.

[52] Y.M. Ha, Y.N. Kim, Y.C. Jung, Rapid and local self-healing ability of polyurethane nanocomposites using photothermal polydopamine-coated graphene oxide triggered by near-infrared laser, Polymers 13 (8) (2021) 1274, https://doi.org/10.3390/polym13081274.

[53] P. Kumar, Harish, G. Andersson, K.M. Subhedar, H.S. Dhami, G. Gupta, A. K. Mukhopadhyay, R.P. Joshi, Utilization of green reductant Thuja Orientalis for reduction of GO to RGO, Ceram. Int. 47 (10) (2021) 14862–14878, https://doi.org/10.1016/j.ceramint.2020.08.063.

[54] A. Pal, B.L. Vernon, M. Nikkhah, Therapeutic neovascularization promoted by injectable hydrogels, Bioact. Mater. 3 (4) (2018) 389–400, https://doi.org/10.1016/j.bioactmat.2018.05.002.

[55] S. Wang, Y. Liu, Q. Sun, B. Zeng, C. Liu, L. Gong, H. Wu, L. Chen, M. Jin, J. Guo, Z. Gao, W. Huang, Triple cross-linked dynamic responsive hydrogel loaded with selenium nanoparticles for modulating the inflammatory microenvironment via PI3K/Akt/NF-κB and MAPK signaling pathways, Adv. Sci. 10 (31) (2023), https://doi.org/10.1002/advs.202303167.

[56] F. Zhang, L.G. Xiong, Y.J. Ai, Z. Liang, Q.L. Liang, Stretchable multiresponsive hydrogel with actuatable, shape memory, and self-healing properties, Adv. Sci. 5 (8) (2018), https://doi.org/10.1002/advs.201800450.

[57] P. Yang, Z. Li, B.R. Fang, L.L. Liu, Self-healing hydrogels based on biological macromolecules in wound healing: a review, Int. J. Biol. Macromol. 253 (2023), https://doi.org/10.1016/j.ijbiomac.2023.127612.

[58] Z. Ling, Z. Chen, J. Deng, Y. Wang, B. Yuan, X. Yang, H. Lin, J. Cao, X. Zhu, X. Zhang, A novel self-healing polydopamine-functionalized chitosan-arginine hydrogel with enhanced angiogenic and antibacterial activities for accelerating skin wound healing, Chem. Eng. J. 420 (2021), https://doi.org/10.1016/j.cej.2021.130302.

[59] R.L. Lu, X.D. Zhou, K. Peng, C. Liu, T. Yuan, P.F. Li, S.Y. Zhang, High-density dynamic bonds cross-linked hydrogel with tissue adhesion, highly efficient self-healing behavior, and NIR photothermal antibacterial ability as dressing for wound repair, Biomacromolecules 25 (4) (2024) 2486–2496, https://doi.org/10.1021/acs.biomac.3c01443.

[60] X. Jing, H.Y. Mi, B.N. Napiwocki, X.F. Peng, L.S. Turng, Mussel-inspired electroactive chitosan/graphene oxide composite hydrogel with rapid self-healing and recovery behavior for tissue engineering, Carbon 125 (2017) 557–570, https://doi.org/10.1016/j.carbon.2017.09.071.

[61] K.C. Wasalathilake, D.G.D. Galpaya, G.A. Ayoko, C. Yan, Understanding the structure-property relationships in hydrothermally reduced graphene oxide hydrogels, Carbon 137 (2018) 282–290, https://doi.org/10.1016/j.carbon.2018.05.036.

[62] D. Aycan, F. Karaca, A. Koca, N. Alemdar, Electro-stimulated drug release by methacrylated hyaluronic acid-based conductive hydrogel with enhanced mechanical properties, Int. J. Biol. Macromol. 231 (2023) 123297, https://doi.org/10.1016/j.ijbiomac.2023.123297.

[63] A.D. Theocharis, S.S. Skandalis, C. Gialeli, N.K. Karamanos, Extracellular matrix structure, Adv. Drug Deliv. Rev. 97 (2016) 4–27, https://doi.org/10.1016/j.addr.2015.11.001.

[64] M.L. Yin, S.S. Wan, X.H. Ren, C.C. Chu, Development of inherently antibacterial, biodegradable, and biologically active chitosan/pseudo-protein hybrid hydrogels as biofunctional wound dressings, Acs Appl Mater Inter 13 (12) (2021) 14701–14712, https://doi.org/10.1021/acsami.0c21680.

[65] J. Li, K. Li, D. Shao, Y. Ding, L. Huang, X. Zheng, The synergistic antioxidant effect of polydopamine coating with amino-functionalized graphene quantum dots on osteoblast protection against oxidative stress, Appl. Surf. Sci. 613 (2023), https://doi.org/10.1016/j.apsusc.2022.155950.

[66] X. Ou, L. Guan, W. Guo, X. Zhang, S. Wu, D. Guo, R. Li, A.V. Zvyagin, Q. Lin, W. Qu, Graphene oxide-based injectable conductive hydrogel dressing with immunomodulatory for chronic infected diabetic wounds, Mater. Des. (2022), https://doi.org/10.1016/j.matdes.2022.111284.

[67] Y. Zhao, Z. Li, S. Song, K. Yang, H. Liu, Z. Yang, J. Wang, B. Yang, Q. Lin, Skin-Inspired antibacterial conductive hydrogels for epidermal sensors and diabetic foot wound dressings, Adv. Funct. Mater. (2019), https://doi.org/10.1002/adfm.201901474.

[68] J. Zhao, J. Li, C. Zhang, F. Hu, H. Wu, X. Man, Z. Li, C. Ye, D. Zou, S. Wang, Design of phase-changeable and injectable alginate hydrogel for imaging-guided tumor hyperthermia and chemotherapy, ACS Appl. Mater. Interfaces 10 (4) (2018) 3392–3404, https://doi.org/10.1021/acsami.7b17608.

[69] L.L. Ma, Y.L. Zhou, Z.W.B. Zhang, Y.Q. Liu, D. Zhai, H. Zhuang, Q. Li, J.D. Yuye, C. T. Wu, J. Chang, Multifunctional bioactive Nd-Ca-Si glasses for fluorescence thermometry, photothermal therapy, and burn tissue repair, Sci. Adv. 6 (32) (2020), https://doi.org/10.1126/sciadv.abb1311.

[70] J.X. Hong, J.Q. Zhu, X.X. Cao, B.Q. Pang, J.R. Xian, X.Q. Yin, Q.Y. Deng, M. H. Chen, Z.Y. Qin, C.Z. Liu, S.N. Varma, Y. Xiao, L. Xiao, M.T. Li, Photo-triggered multifunctional gold-based hybrid nanoflowers promote infectious skin regeneration, Chem. Eng. J. 482 (2024), https://doi.org/10.1016/j.cej.2024.148937.

[71] Y.P. Liang, X. Zhao, T.L. Hu, B.J. Chen, Z.H. Yin, P.X. Ma, B.L. Guo, Adhesive hemostatic conducting injectable composite hydrogels with sustained drug release and photothermal antibacterial activity to promote full-thickness skin regeneration during wound healing, Small 15 (12) (2019), https://doi.org/10.1002/smll.201900046.

[72] H.D. Zomer, T.D. Jeremias, B. Ratner, A.G. Trentin, Mesenchymal stromal cells from dermal and adipose tissues induce macrophage polarization to a pro-repair phenotype and improve skin wound healing, Cytotherapy 22 (5) (2020) 247–260, https://doi.org/10.1016/j.jcyt.2020.02.003.

[73] T.J. Keane, C.M. Horejs, M.M. Stevens, Scarring vs. functional healing: matrix-based strategies to regulate tissue repair, Adv. Drug Deliv. Rev. 129 (2018) 407–419, https://doi.org/10.1016/j.addr.2018.02.002.